COMPUTATIONAL AERODYNAMICS OF HOVERING HELICOPTER ROTORS

Nik Ahmad Ridhwan Nik Mohd[*1] and George N. Barakos[2]

[1]Faculty of Mechanical Engineering,
Universiti Teknologi Malaysia,
81310 Skudai, Johor, Malaysia

[2]CFD Laboratory, University of Liverpool,
Liverpool, L69 3GH, UK

ABSTRACT

The computation of rotor flowfields is a challenging problem in theoretical aerodynamics and essential for rotor design. In this paper we discuss the prediction of rotor hover performance, wake geometry and its strength using CFD methods. The benefits and differences between simple, momentum-based source-sink models and truncated vortex-tube far-field boundary conditions on the rotor flowfield modelling, and the convergence of the numerical solution are investigated and presented. Helicopter rotors in axial flight are simulated using the Helicopter Multi-block (HMB2) solver of the Liverpool University for a range of rotor tip speeds and collective pitch settings. The predicted data were then compared with available experimental data and the results indicates that, blade loading and wake geometry are in excellent agreement with experiments and have moderate sensitivity to the grid resolution. The work suggests that efficient solutions can be obtained and the use of the momentum theory is essential for efficient CFD computations.

Keywords: *CFD, hovering, rotor wake, RANS, source-sink, vortex-tube*

1.0 INTRODUCTION

Accurate prediction of rotor wakes is known as an important component for the overall rotor aerodynamic loads and performance analyses. Almost all aerodynamic design problems associated with rotorcraft involve estimates of the blade loading and the wakes. The nature of the rotor wake in terms of its geometry, strength and the aerodynamic effects it induces, depends principally on the operating state and flight conditions of the helicopter. In hover, the tip vortices stay below the rotor plane in close proximity to the rotor blades for appreciable time. These vortical structures are convected away at relatively low speeds even at higher thrust settings and induce significant flow on the rotor blades leading to substantial changes in blade angle of attack and airloads. Computational fluid dynamics (CFD) has been used as a flow analysis tool for many years. However, the ability of CFD methods to predict the rotor wakes with good of accuracy still remains an important research area. Poor results for wake prediction are often associated with the rapid diffusion and dispersion of the tip vortices on coarse CFD meshes. The results improve on finer grids, however, will increase the computational time. Consequently, in

---

[*]Corresponding author : ridhwan@fkm.utm.my

order to capture the rotor tip vortices at high degree of accuracy, several efforts have been reported in the literature. Different meshing strategies (e.g., overset grid [1,2]), implementation of high order CFD schemes [3], development of rotor flow solvers based on the finite element [4], vortex methods [5], and hybrid CFD and vortex methods [6,7] are among of the methods that have high intention in rotorcraft wake prediction recently.

Apart from that, the selection of the far-field boundary and initial conditions to model the general characteristics of the rotor flow field is yet another important aspect in rotorcraft CFD that needs to be considered. So far, there is no unique method for specifying far-field conditions. However, most rotorcraft CFD simulations use a far-field condition with the assumption of quiescent initial conditions outside the computational domain where the flow into and out of the domain will be zero [8]. This creates an environment similar to many hover test chambers. The use of this far-field boundary condition requires a large computational domain and is not cost effective due to the large number of mesh points needed for wake capturing. An alternative to that, a far-field boundary condition which assumes that a non-zero flow at far-field boundary conditions, and allows the flow to enter and leave the domain without changing the conservation laws was introduced by Srinivasan [8]. This far-field model allows the use of smaller computational domains but its application is limited to hover computations.

The raise of interest in new far-field boundary conditions based on the truncated vortex tube model provides a new choice for rotor flow prediction [9]. The advantage of the vortex tube model is that not only it can be used in hover but can easily be extended to climbing and descending flight conditions. An extensive analysis of hovering rotor flow was reported by Choi et.al.[10,11] They showed that a more stable wake structure and faster convergence of CFD solutions can be obtained using the vortex-tube boundary and initial conditions even with a smaller computational domain. The improvements in the wake structure and the solution convergence are due to the vortex-tube model that allows the starting vortex to go through the outflow domain boundary which is not the case in the source-sink model. Using a smaller computational domain and retaining the number of mesh points is the simplest approach to improve the mesh resolution in the areas of interest.

To accurately assess the aerodynamics of any model rotors, experiments of high quality are needed to provide data for the loads on the blades as well as the structure of the wake. Such a work was carried-out by Caradonna and Tung [12,13] They measured the wake properties (geometry and strength) of hovering, 2-bladed, rectangular model rotors of low and high aspect ratios using hot wire anemometry. In recent years, the ability to quickly survey larger regions of the flow using the Laser Doppler Velocimetry (LDV), or using the particle image velocimetry (PIV) technique has also become increasingly viable and is now effective tool for studying rotor wakes [14]. A more complex rotor blade, the 4-bladed, ONERA 7AD1 model rotor with anhedral and swept tip has also been simulated to provide data for validation. The work of Caradonna [15] on the vertical climb flight of the 2-bladed, UH-1H model rotor was also employed for validation. The current work presented in this paper is an effort to assess the far-field boundary conditions for rotors flow in hover and vertical flight using the simple, momentum-based source-sink and the vortex-tube far-field boundary conditions. The influence of the different far-field boundary models and CFD domain size on the rotor aerodynamic loads, wake geometry and strengths will be analysed and compared with the available experimental data. The effect of the far-field boundary conditions was firstly estimated using simple momentum theory and this is followed by detailed analysis using the Helicopter Multi-block (HMB2) solver of Liverpool University.

2.0   NUMERICAL METHODS

2.1   Simple Momentum Theory

The choice of boundary conditions for a given problem must respect flow physics and must be compatible with the characteristic wave propagation theory for the Euler and Navier-Stokes equations [11]. The correct selection of the conditions for the far-field boundary results in better prediction of the blade loads, wake geometry and faster convergence to the solution. In general, the flow field at an initial stage of the computation is unknown and must be initialised to some reasonable conditions. Many hovering computations assume a quiescent flowfield around the rotor. However, a large computational domain is required to resolve the recirculation of flow induced below the rotor disk. As an initial assessment, the far-field boundary conditions based on the source-sink[8] and truncated vortex tube [9,10] models were computed using simple momentum theory. The rotor and test case considered is the low aspect ratio Caradonna and Tung rotor in hover at $C_T = 0.009$ and tip Mach number of $M_{tip} = 0.612$. The computations were performed in a 3-dimensional, cylindrical type domain, single block with structured mesh topology.

2.2   Source-sink Model

The source-sink far-field model was first introduced by Srinivasan [8] and remains widely used for rotor hover simulations [2,16,17] According to this far-field boundary model, the rotor flow field is computed using a three- dimensional source-sink singularity, with a strength determined from the rotor thrust and simple momentum theory. The singularity is located on the rotor axis of rotation and at the rotor disk plane. The point-sink pulls the flow from the surrounding into the computational domain resulting in a velocity given by

$$\overline{W}_{in} = -\frac{1}{8}\sqrt{C_T}\left(\frac{R}{d}\right)^2 \tag{1}$$

where $d_p^2 = x_p^2 + y_p^2 + z_p^2$ is the distance of an arbitrary point (x_p, y_p, z_p) from the rotor centre of rotation. Equation 1 gives the magnitude of the total incoming velocity normalised with rotor tip speed, V_{tip}. An appropriate component of this flow enters the computational domain from each boundary except through an exit plane on the lower boundary (see Figure 1a). Assuming that the far-field exit velocity is uniform, its magnitude can be determined from 1-D momentum theory by relating the outflow momentum to the rotor thrust coefficient, C_T by :

$$\overline{W}_{out} = \begin{cases} -\sqrt{C_T} \text{,Srinivasan [8]} \\ -\sqrt{\dfrac{C_T}{4}} \Big/ \left(\dfrac{R_{out}}{R}\right)^2 \text{,Srinivasan modified[16]} \end{cases} \tag{2}$$

The radius of the outflow region is empirically set as:

$$R_{out} = \begin{cases} 1.12R/\sqrt{2} \text{,Srinivasan [8]} \\ R(0.78 + 0.22e^{H_{out}/R}) \text{,Srinivasan modified [16]} \end{cases} \tag{3}$$

where the rotor thrust coeffcient is defined as $C_T = 2T / \rho\pi R^2 V_{tip}$. This model will be referred to as Model 1. A slightly different expression of the outflow velocity and outflow radius were implemented in the HMB2 solver where the radius of outflow boundary is accounted for in the outflow velocity calculation and the distance from the rotor plane to the outflow boundary is accounted for in the outflow boundary calculation. A schematic showing this set of boundary conditions is given in Figure 1a. This simple flow model provides a reasonable approximation of the actual rotor flow and allows for a smaller computational domain than what would be required if zero velocity, ambient pressure conditions were prescribed [8]. For the CFD analyses, estimated C_T values are used to initially set the boundary condition.

2.3 Vortex-Tube Model

The second type of outer boundary model for rotor flow field is based on the simplifying assumption about the nature of the mean flow through the rotor introduced by Wang[9]. This assumption leads to a simple representation of the rotor wake by a truncated vortex tube of continuously distributed vorticity (see Figure 1b). In this model, it is assumed that the circulation Γ of the trailing vortices decays linearly. The distance required for the circulation to decay to zero is assumed to be directly proportional to the mean (average) transport velocity of trailing vortices.
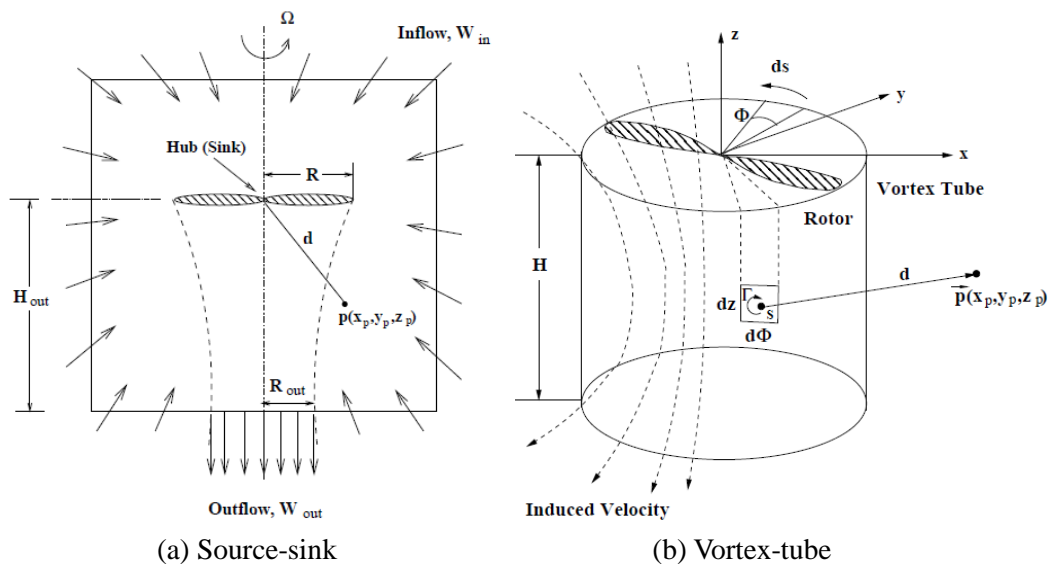

| (a) Source-sink | (b) Vortex-tube |

Figure 1 :   Schematic of the source-sink (Adapted from Srinivasan[8] and the vortex tube models (Adapted from Choi et.al.[10,18])

In the vortex tube model, the rotor is modelled as a disk at its inlet, and the vorticity trailed from the blade tips is spread evenly down the tube [9]. Consider a small vortical element at point *s = (R cos φ, R sin φ)* on the vortex tube surface with strength, *Γ* per unit length circumferentially and axially down the tube. Integrating along the azimuthal and axial directions for the entire truncated vortex tube, the velocity at any arbitrary point $p(x_p, y_p, z_p)$ in space, induced by element *Γds* located at a point s, can be expressed in a vector form given by Equation 4. The upward displacement, velocities and forces are assumed positive. Since the hover flow has axial symmetry, the solution in the x_p direction represents any azimuth angle.

Vortex tube models not only can be used to hovering flight but can easily be implemented to other axial flight (climb and descent) conditions [9,10]. The models require some numerical integration and represent a first-order approximation of the

detailed rotor wake. Starts from the Biot-Savart law:

$$\vec{v}(p) = \frac{\Gamma \, dz}{4\pi} \frac{\vec{ds} \times \vec{d}}{\left|\vec{d}\right|^3}$$

(4)

$$\vec{p} = \vec{x}_p \vec{i} + \vec{y}_p \vec{j} + \vec{z}_p \vec{k}$$
$$\vec{s} = \vec{R}\cos\phi \vec{i} + \vec{R}\sin\phi \vec{j} + \vec{z}\vec{k}$$
$$\vec{d} = \vec{p} - \vec{s} = (\vec{x}_p - \vec{R}\cos\phi)\vec{i} - \vec{R}\sin\phi \vec{j} + (\vec{z}_p - \vec{z})\vec{k}$$
$$\vec{ds} = -\vec{R}\sin\phi d\,\phi \vec{i} + \vec{R}\cos\phi d\,\phi \vec{j}$$

(5)

and after integration, the radial and axial velocity normalised with the induced velocity and as a function of the vortex tube length, $\overline{H}$ can be expressed by the following equations[10]:

$$\vec{v}_r(p) = -\int_0^{\overline{H}} \int_0^{2\pi} \frac{1}{2\pi \vec{V}_t} \frac{f_\gamma(\vec{z})[(\vec{z}_p - \vec{z})\cos\phi]}{[\vec{x}_p^2 + 1 - 2\vec{x}_p \cos\phi + (\vec{z}_p - \vec{z})^2]^{3/2}} d\phi \, d\,z$$

(6)

$$\vec{v}_z(p) = -\int_0^{\overline{H}} \int_0^{2\pi} \frac{1}{2\pi \overline{V}_t} \frac{f_\gamma(\vec{z})[1 - \vec{x}_p \cos\phi]}{[\vec{x}_p^2 + 1 - 2\vec{x}_p \cos\phi + (\vec{z}_p - \vec{z})^2]^{3/2}} d\phi \, d\,z$$

(7)

$\overline{V}_v$, $\overline{H}$ and $\overline{V}_t$ are the axial climb velocity, the vortex tube length, and the total transport velocity normalised with the rotor axial induced velocity, $\overline{v}_i$:

$$\overline{V}_v = \frac{\overline{H}}{k_H} + \frac{k_H k'_t A'}{2\overline{H}}(\sqrt{\overline{H}^2 + 1} - 1)$$

(8)

$$\overline{H} = \overline{k_H V_t}, \qquad \overline{v}_i = \frac{-A' f(\overline{H})}{\overline{H}/k_H}, \qquad and \ f(\overline{H}) = \frac{\sqrt{\overline{H}^2 + 1} - 1}{\overline{H}}$$

(9)

where,

$$\overline{V}_v = \frac{V_v}{v_{i_{hov}}}, \qquad \overline{v}_{i_{hov}} = -\frac{\sqrt{C_T}}{2} V_{tip}, \qquad and \ C_T = \frac{T}{\frac{1}{2}\rho R^2 V_{tip}^2}$$

(10)

The values for k_H, k_t' and A' may be selected to suit various tests[9]. These were obtained empirically [19], and are given below:

$$k_H = 3, \qquad A' = 1.62, \qquad k'_t = 2 - 0.8\exp^{[-(\overline{H}/2)^2]}$$

(11)

The vortex tube model can have a constant or linearly reduced vortex strength by substituting $f_\gamma(z)$ in Equations 6 and 7 with the following options [11]:

$$f_\gamma(\bar{z}) = \begin{cases} 1 & , \quad \text{Constant vortex strength} \\ 1 - \dfrac{\bar{z}}{\bar{H}} & , \quad \text{Linear \quad vortex strength} \end{cases} \tag{12}$$

Figure 2(a) shows plots of the rotor induced velocity, $\bar{v}_i$ against rotor vertical speed, $\bar{V}_c$ at different descending flight conditions from Wang [9]. The values of these parameters are given in Table 1. Furthermore, using Equations 7 – 12, it is possible to extend the plot to climb state (Figure 2(b)). Figure 2(b) relates the length of the truncated wake to $\bar{V}_v$ and flight conditions.

3.0 CFD FLOW SOLVER

The Helicopter Multi-block (HMB2) [16,20] solver has been used for rotor aerodynamic calculations. HMB2 is a computational fluid dynamics Navier-Stokes solver developed at the CFD Laboratory of the University of Liverpool and runs on parallel distributed memory computers. HMB2 solves the 3D Unsteady Reynolds Averaging Navier-Stokes (URANS) equations on multi-block structured meshes using a cell-centred finite-volume method for spatial discretisation. The convective terms are discretised using either Osher's or Roe's scheme. Monotone Upstream-centred Schemes for Conservation Laws (MUSCL) interpolation is used to provide formally third order accuracy in the calculation of fluxes. The Van Albada limiter is used to avoid spurious oscillation in the flow properties across shocks by locally reducing the accuracy of the numerical scheme to first order. The resulting linear system of equations is solved using a pre-conditioned Generalised Conjugate Gradient method in conjunction with a Lower Upper factorisation. For unsteady simulations, implicit dual-time stepping is used based on Jameson's pseudo-time integration approach.

The calculated hovering rotor flow simulations were performed by assuming that the wake shed from the rotor is steady. The hover formulation [16] of HMB2 allows the computation of hovering rotor flows to be treated as steady-state cases. The formulation uses a mesh that does not rotate and employs a transformation of the frame of reference to account for the rotation. The viscous computations in the current work were performed using the standard $\kappa - \omega$ turbulence model of Wilcox [21]. Furthermore, the solver has been used and validated for several fundamental flows apart from rotor cases [20,22].

Table 1: Estimates of hover parameters from Wang [9].

$\bar{H}$	-3.24	-3.0	-2.4	-2.8	-1.2	-0.6	0
$\bar{V}_v$	0	0.12	0.42	0.71	0.97	1.22	1.46
$\bar{v}_i$	-1.08	-1.17	-1.35	-1.59	-1.90	-2.24	-2.46
$\bar{H}$	0.6	1.2	1.38	1.8	2.4	3.0	3.6
$\bar{V}_v$	1.62	1.77	1.8	1.91	2.02	2.12	2.21
$\bar{v}_i$	-2.24	-1.90	-1.8	-1.59	-1.35	-1.17	-1.03
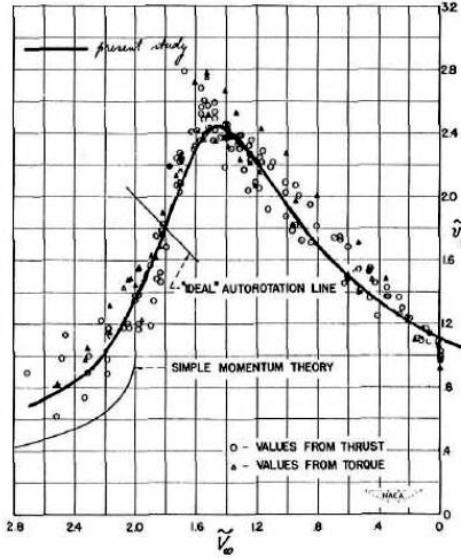
(a) Plot for axial flight conditions from Wang [9]
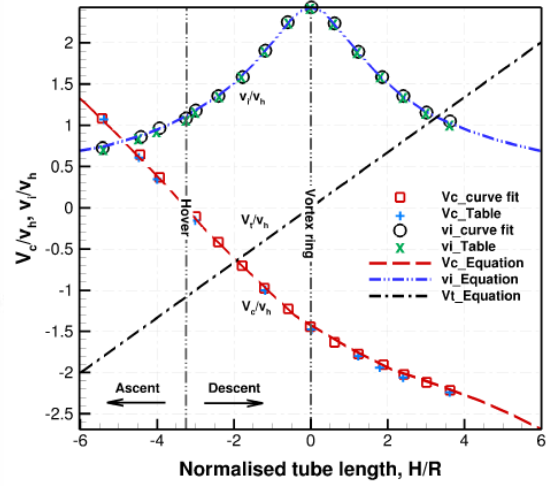
(b) Axial flight conditions as a function of the vortex-tube length

The governing equations of the HMB2 are the unsteady three-dimensional compressible Navier-Stokes equations, written in dimensionless form as:

$$\frac{\partial Q}{\partial t} + \frac{\partial}{\partial x}(\boldsymbol{F}^{inv} + \boldsymbol{F}^{vis}) + \frac{\partial}{\partial y}(\boldsymbol{G}^{inv} + \boldsymbol{G}^{vis}) + \frac{\partial}{\partial z}(\boldsymbol{H}^{inv} + \boldsymbol{H}^{vis}) = \vec{S} \tag{13}$$

where Q contains the unsteady terms and $\boldsymbol{F}$, $\boldsymbol{G}$ and $\boldsymbol{H}$ are spatial flux vectors in x, y, z directions expressed in terms of transformed velocities U, V, W for the rotating frame of reference for hover cases. The terms have been split into their inviscid (*inv*) and viscous (*vis*) parts. Source terms are denoted by S and contain entries for turbulence models volumetric terms.

3.1   Hover Formulation

Assuming the wake shed by the rotor is periodic in space and time, the flow around a hovering rotor can be treated as a steady-state problem. Moreover, domain periodicity in the azimuthal direction is employed to reduce computational time. So, with the periodic boundaries, an n-bladed rotor can be approximated using a $1/n$ domain segment. For hover in the x-y plane at a constant rotation rate ω, the rotation vector about the z-axis can be:

$$\vec{\omega} = (0, 0, |\omega|)^T \tag{14}$$

A non-inertial frame of reference is used to account for the rotor rotation. Both the centripetal and Coriolis acceleration terms in the momentum equations are accounted for using a combination of a mesh velocity in the formulation of the Navier-Stokes equations and a source term for the momentum equations. The mesh velocity introduced is essentially the mesh rotation velocity:

$$\vec{u}_{ref} = \vec{\omega} \times \vec{r} \tag{15}$$

In addition to the mesh velocity, a source term for the momentum equations is introduced:

$$\vec{S} = [0, -\rho|\omega| \times \vec{u}_h, 0]^T \tag{16}$$

where *r* is the position vector of the cell and uh is the velocity field in the present rotor-fixed frame of reference.

4.0 CFD MESH GENERATION

Mesh generation and mesh quality are of fundamental importance in all aerodynamics simulations and even more in rotorcraft. Modelling the rotor flow field with wake capturing requires meshes with varying characteristics. In rotorcraft simulation, the requirement is to maintain mesh quality in the far-field of the computational domain so as to adequately capture the rotor wake over large distances away from rotor disk. The employed CFD method requires multi-block structured meshes and in the current work all meshes and blade geometries were generated using the ICEM-HEXA package, and then converted into a format suitable for the HMB2 solver. In HMB2 the hovering rotor flow field is assumed to be symmetric and periodic in time. This allows the generation of a computational domain of a single blade and significantly reduces the number of required mesh points.

The details of the structured C-H-H CFD meshes constructed around a hovering rotor blade are shown in Figure 3. An H-type structure is used away from the blades with a C-type structure attached to them. This type of mesh topology allows for accurate viscous case computation and also provides a mechanism for pitching the blades, with the near-blade mesh remaining in an undeformed state[17]. For all meshes, viscous spacing in the direction normal to the blade surface with the first cell located at $10^{-5}c$ above the blade and exponential distribution was employed. For viscous cases, and for the Reynolds number in Table 2, this mesh spacing results in $y^+ < 1$.

The rotor centre of rotation is located at the *z*-axis, the rotor blade is laid on the *x*-axis and the quarter chord point is taken at *y*=0 with the blade leading edge pointing at the positive *y*-axis. This geometry was used for the construction of the computational meshes for the Caradonna and Tung model helicopter rotors [12,13]. The rotor hub was modelled as a simple straight cylinder. CFD mesh of low and high resolution below and near the rotor tip region was constructed to see its influence on the tip vortex visualisation. For Navier-Stokes calculations, these coarse mesh sizes were found to be adequate for blade loading predictions. However, for accurate wake visualisation and wake trajectory predictions, the fine mesh resolution is required since this reduces the diffusion and dispersion problems occurring on the coarse mesh.
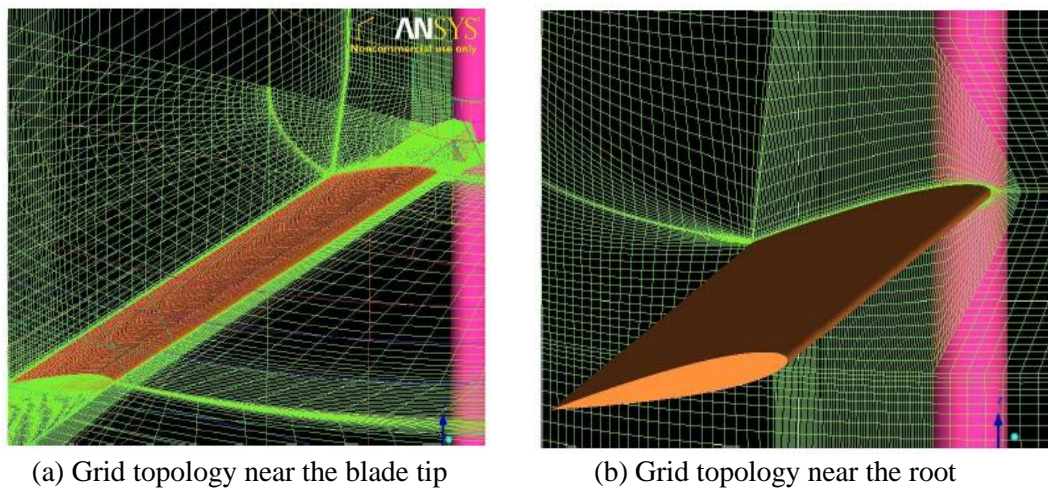

(a) Grid topology near the blade tip   (b) Grid topology near the root

Figure 3: Multi-block meshing near the tip and root of the blade

4.1 Hovering Rotors

Caradonna and Tung [12,13] carried-out experimental and analytical studies of model helicopter rotors in hover. The experimental study involves the blade pressure measurements, tip vortex geometry surveys and measurements of vortex strength [12]. In the wind tunnel experiments of Caradonna and Tung [12,13], the rotors were mounted on a tall column containing the drive shaft in the centre of a chamber, and the tunnel was equipped with special ducting to eliminate room recirculation. The pressure and loads at different blade stations on the blade surface of a low aspect ratio blade were obtained from 60 pressure tubes [12]. A six- component balance was used to measured the loads for the high aspect ratio blade [13]. The wake strength and geometry data were acquired using a traverse hot-wire probe mounted below the rotor. To exclude the effect of the axial velocity on the induced velocity measurement and also the magnitude of the vortex induced velocity is properly measured, the hot-wire probe placed tangent to the rotor tip path. The tip vortex geometry and strength data were acquired from various point along the tip vortex trajectories.

The ONERA 7AD1 rotor was also used in this work. This rotor was designed and tested by ONERA in the DNW wind tunnel during the HELISHAPE research campaign [16]. This rotor is a high aspect ratio (AR = 15) four-bladed design of 2.1 m radius, and 0.41 m chord. The rotor blade has a linear geometric twist and uses the ONERA 213 aerofoil profile from root to 0.7R and the ONERA 209 aerofoil profile from 0.9R to the tip. The blade tip was designed with sweep, and anhedral. In HMB2, inviscid flow was used to simulate the 7AD1 rotor in hover at a tip Mach number of $M_{tip} = 0.6612$. Results presented are shown for a collective pitch setting of 7.5^o.

4.2 Rotors in Vertical Climb

The experimental measurement of helicopter rotor performance and wake in hover and low-speed axial flight was also reported by Caradonna [15]. The model rotor used in the experimental measurements was the two- bladed, Bell profile, UH-1H model rotor with a teetering hub, and full swashplate control. To achieve a low freestream condition for the climb case and to reduce the wall effect by the chamber size, the model rotor was mounted in the settling chamber of the 7'x10' No. 1 wind-tunnel at Ames Research Centre by orienting the rotor axis horizontally. In that work, the blade tip Mach number was set to constant ($M_{tip} = 0.5771$), but the blade collective pitch and tunnel speed were varied to simulate different climb speeds. The wake of the rotor in hover and vertical climb was visualised using smoke injected far upstream of the disk (for overall wake region) and single-point smoke (for tip vortices visualisation) of the rotor and a white light-sheet system. It was also reported that for the low climb speed region and the hover case, the measured figure of merit (FM) versus the rotor rate-of-climb was affected by the flow unsteadiness causing the FM to reduce as hover was approached, before it decreased steeply with increased climb rate (axial velocity). The true hover performance was obtained by extrapolating the linear climb trend to zero climb-rate. The UH-1H rotor performance was also compared with the HELIX-I code [15]. The summary of the blade geometry and flow conditions used in the present works are given in Table 2.

In CFD simulations, trimmed solutions are essential when making comparisons with experimental data. Trimming leads to a balance of aerodynamic, inertial and gravitational forces and moments about the rotating axes. The trimming method used here is based on the momentum theory and approximated rotor aeromechanics [16,23]. The trim state of the rotor in hover and vertical climb were obtained by approximating the increment in the blade collective pitch angle ($\Delta\theta_o$) required to climb and to maintain the thrust at about as required for hover. In the CFD grid, an initial blade collective of 11° and 0° of coning were used. The grid trimmer utility of HMB was then applied to alter the blade collective angle by rotating the C-part of the mesh bounding the blade. For

simulations of trimmed rotors, the trimming was carried-out after a steady flow solution has converged to a prescribed residual.

5.0 VATISTAS VORTEX MODEL

Apart from experiments, flow models can also be compared with CFD to obtain more insight in the validity of the CFD results. The wake contraction and the diffusion of the vortex core can be modelled using several available empirical methods. In this section, the decay of the tip vortex trailed behind a hovering low aspect ratio Caradonna-Tung [12] model rotor was demonstrated using the empirical velocity profiles of Vatistas et.al. [24] The Vatistas vortex profile used in this analysis is generated in 2D using input parameters obtained from the HMB2 simulations. Different Vatistas fit parameters were used and compared with HMB2 results. Vatistas et.al. [24] derived a general expression that encompasses a series of tangential velocity profiles for vorticity:

$$\overline{V_\theta} = f_n(\overline{r}) \tag{17}$$

Where $\overline{V_\theta} = 2\pi r_c V_\theta / \Gamma_\infty, \overline{r} = r/r_c, r_c$ is the core radius, $\overline{V_\theta}$ is the tangential velocity, and Γ_∞ is the vortex circulation. The non-dimensional empirical formulation for the tangential velocity component is given by the expression:

$$\overline{V_\theta} = \frac{\overline{r}}{(1+\overline{r}^{2n})^{1/n}} \tag{18}$$

n is a fit parameter (positive integer), and r is the local radial coordinate with respect to the vortex centre. The dimensionless radial velocity components can be obtained from the angular, θ-momentum equation (Equation 18) with the assumption that in the concentrated vortex, the azimuthal velocity does not depend strongly in the axial direction[24]. This gives

$$\overline{V_r} = \frac{2(1+\overline{r}^{2n})^{1/n}}{1+\overline{r}^{2n}} \tag{19}$$

Where $\overline{V_r} = V_r r_c / v, v = 1.455 \times 10^{-5}$ m^2/s is the kinematic viscosity of ambient air at standard sea level. For a fit parameter of, n = 1, the velocity distribution is similar to the Scully vortex profile [25]. Vatistas et.al. suggested that the n = 2 profile gives a tangential velocity profile similar to the Burger's vortex, and the Rankine profile can be obtained for $n = \infty$. The Cartesian *u*- and *v*-velocity components at any arbitrary point can then be obtained by transforming the tangential and radial velocity components to the Cartesian system. Therefore, from the known velocity components, vorticity can be calculated from the vorticity-velocity relationship

$$\vec{\omega} = \nabla \times \vec{u} \tag{20}$$

6.0 RESULTS AND DISCUSSION

6.1 Results of Simple Momentum Theory
At first, an evaluation is presented for the source-sink and vortex tube boundary and initial conditions of a hovering rotor flow simulation at steady-state condition using a

simple momentum theory. The test case used for this demonstration is similar to the low aspect ratio, Caradonna and Tung model rotor for the test case of $M_{tip} = 0.612$ and $C_T = 0.009$. The rotor has AR = 6.0, and the size of the computational domain in all directions used in the current analysis was the same size as used for CFD simulations except that a slightly longer inflow domain boundary was used mainly for descending rotor flow simulations. The rotor centre of rotation is located at $z/c = 0$ and $x/c = 0$. Figures 4 to 6 show the plot of streamlines, vorticity and induced velocity profile computed using the simple momentum models.

|(a) Source-sink | (b) Vortex tube with constant vortex strength | (c) Vortex tube with linearly reduced vortex strength |
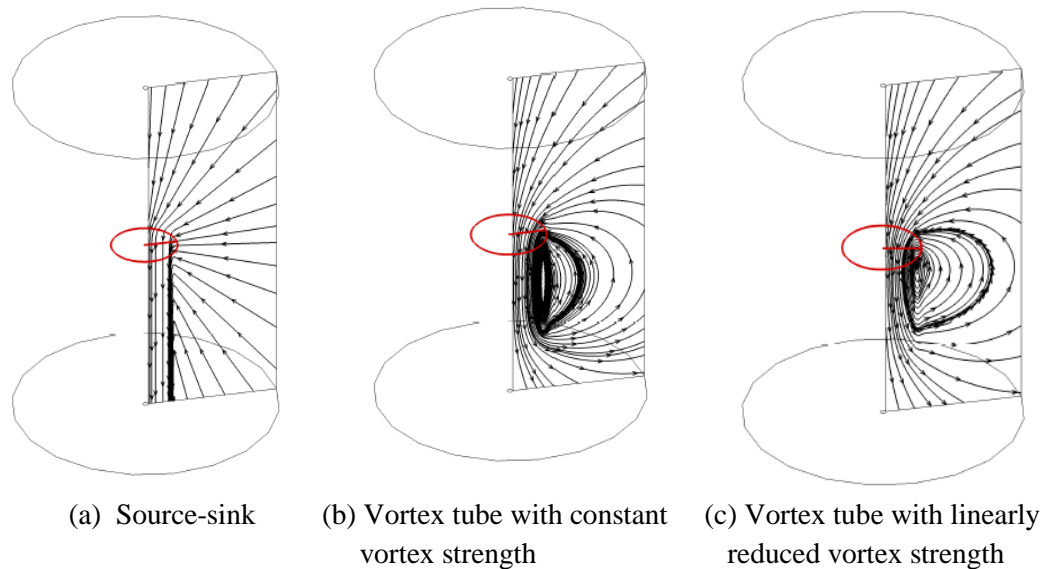
Figure 4 : Streamlines for hovering rotors obtained from different far-field boundary models.

Looking at the hovering rotor flowfield modelled using the source-sink model, the surrounding flows is pulled into the computational domain towards the point-sink located at the rotor hub (Figures 4(a)) and then induced straight downstream to the outflow boundary. In Figures 4(b) and (c) furthermore, the flowfield below the rotor plane recirculate forming the starting vortex. A similar flow can be seen in Figure 5 with the regions of high vorticity magnitudes visualized. The distribution of the induced axial velocity extracted above and below the rotor plane modelled using ths source-sink models is shown in Figures 6(a) and (b). The induced axial velocities below the rotor plane are relatively small far from the rotor disk, increase rapidly towards the rotor tip and then reach a constant magnitude of the axial velocity below the rotor plane. Above the rotor plane however, the induced axial velocity remains small for the typical test case demonstrated here. As a comparison, the source-sink models of Srinivasan [8] and a modified Srinivasan used in the HMB2[16] show similar flow patterns.

However, the modified Srinivasan model induced a slightly higher magnitude of axial velocity compared to the original. For the vorticity distributions (Figures 5(a) and (b)), the source-sink model induced a constant vorticity below the rotor plane in the blade tip region that extended to the outflow boundary of the computational domain. The assumption of a constant outflow boundary is also not accurate enough since the radius of the slipstream boundary varies with the distance of the rotor disk to the outflow boundary. From this analysis, it is shown that the initial flow condition obtained using the source-sink model does not represent a real rotor flow and requires a large computational domain.

(a) Source-sink model (HMB) (b) Source-sink model (Srinivasan [8])

(c) Vortex-tube
(constant vortex strength)

(d) Vortex-tube
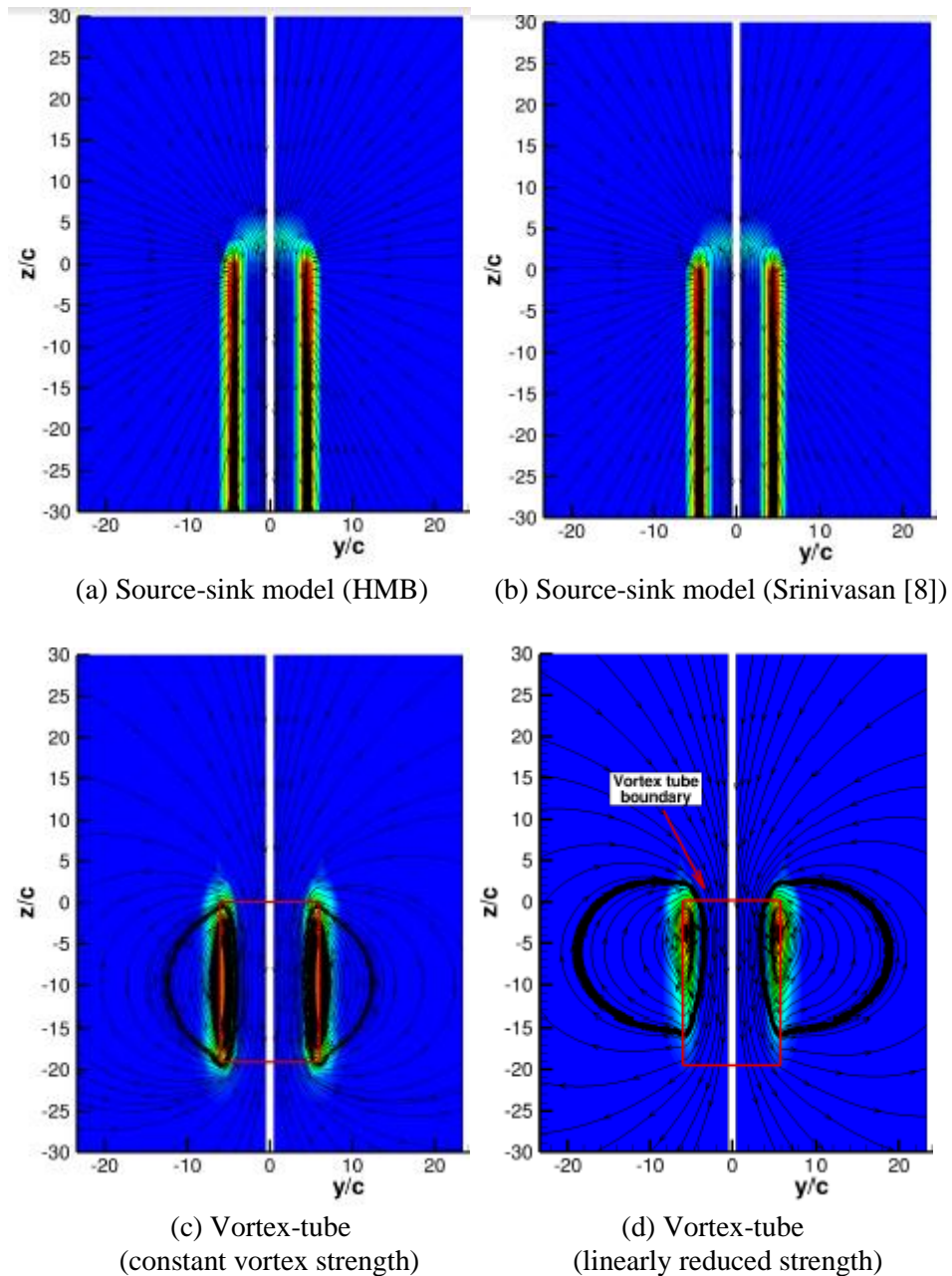(linearly reduced strength)

Figure 5 : Contour of vorticity of various momentum theory models.

In the vortex tube model, the flowfield residing outside the vortex tube is initially assumed at rest. It is then disturbed by the flowfield containing high speed downwash velocity induced by the rotor that is located in the vortex tube boundary. This results in a large recirculating flow generated below the rotor plane as shown in Figures 4(b) and (c). In these models and as shown in Figures 5(c) and (d), the vorticity induced by the rotor does not extend to infinity as in the source-sink model but is truncated as it travels downstream the rotor plane disk (Figures 5(c) and (d)). The radius of the outflow boundary also seems much larger in the vortex tube models and varies with the distance from rotor disk to the outflow boundary.

In terms of the vorticity field, for the vortex tube with constant vortex strength, the rotor induces a constant magnitude of vorticity in the near tip region and below the rotor plane as in the source-sink model but the strength of vorticity induced by the rotor truncated itself at a distance below the rotor disk (Figure 5(c)). A better vorticity

distribution however, can be seen in the vortex tube model with linearly reduced vortex strength where the strength of vorticity decays gradually as it travels downstream of the rotor disk (Figure 5(d)).

The distributions of the induced axial velocities of the vortex tube models taken at various stations above and below the rotor planes are plotted in Figures 6(c) and (d). As for the source-sink model, the rotor in the vortex tube model induced a relatively small axial velocity far from the rotor. However, a higher magnitude of velocity can be seen in the near tip region as compared to the source-sink model. The induced axial velocity of the constant strength vortex tube shows almost the same magnitude of induced velocity at 1R and 2R below the rotor plane and an abrupt drop between 3R and 4R. A more evenly distributed downwash can be obtained from the vortex tube with linearly reduced vortex strength. This shows the capability of the linearly reduced vortex model to better approximate the real rotor flow. From these demonstrations, it is expected that the vortex tube model with linearly reduced vortex strength is perhaps better for simulating the rotor flowfield compared to the source-sink and vortex tube with constant vortex strength models.

For a further demonstration, a hovering rotor flowfield was computed using URANS CFD. The differences in the flowfield pattern modelled using the first- and high-order spatial accuracy are observed and highlighted. Using the high order spatial accuracy, the CFD solution is capable of capturing the details of flowfield including the formations of the tip vortices as shown in Figure 7(b). The flowfield computed using the first order spatial accuracy CFD solution however, resembles the vortex tube models with the starting vortex flow recirculation appears below the rotor plane. This is a positive result suggesting that the vortex tube model has potential as a boundary condition for CFD.
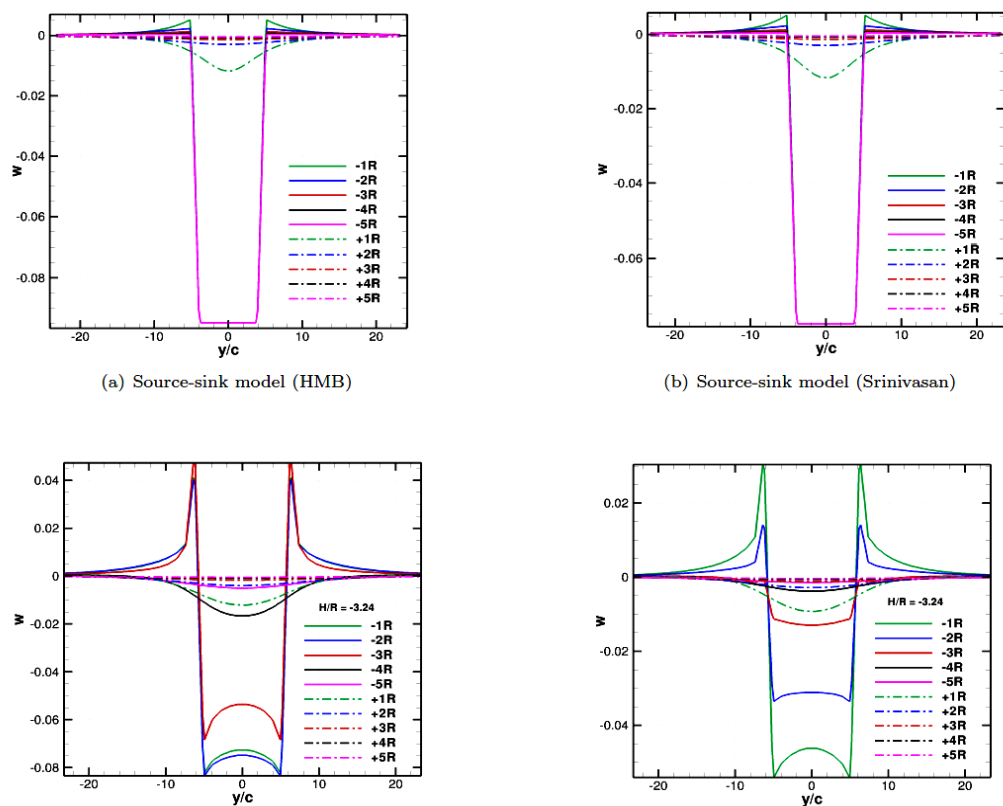

(a) Source-sink model (HMB)

(b) Source-sink model (Srinivasan)

Figure 6 : Induced velocity profile of various momentum theory models (above (+ve) and below (-ve))

(a) 1st order spatial accuracy solution   (b) High order spatial accuracy solution
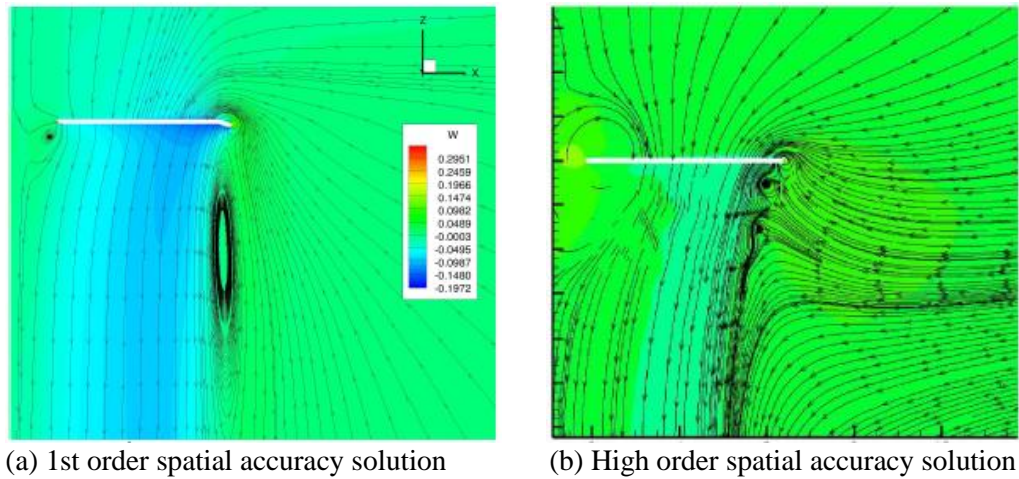
Figure 7 : Hovering rotor flowfield for different spatial accuracy solutions.

6.2   Results for the Caradonna and Tung Rotors in Hover

In this work, Model 1 of the source-sink boundary condition was used and calculations were performed using the $\kappa - \omega$ turbulence model of Wilcox [21]. Figure 8 shows the convergence of the CFD solution for a typical case. In the HMB2 calculations, the convergence criterion for all test cases was set to 10^{-8} of the L_2 norm of the residual. Typical calculations were run for up to 50,000 iterations, although thrust, torque and figure of merit show little change after 10,000 iterations.

(a) Thrust coefficient   (b) Torque coefficient
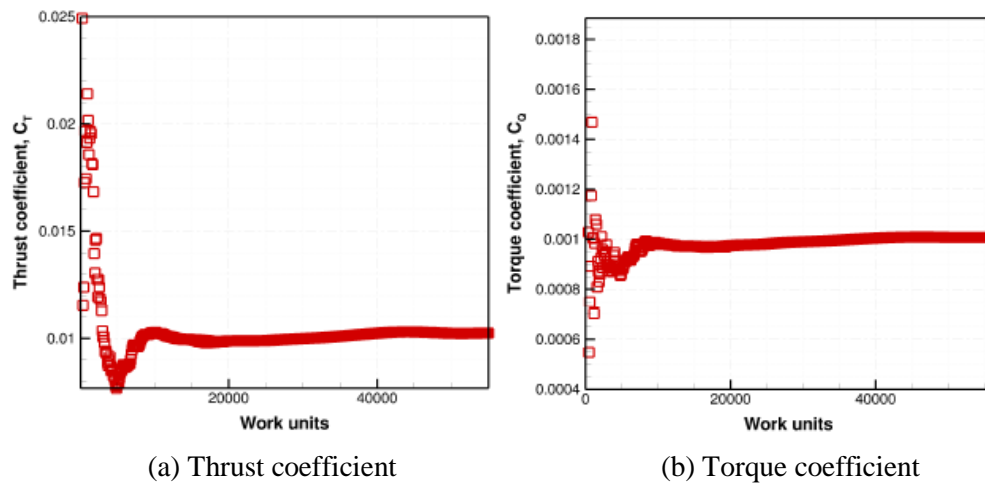
Figure 8 : Convergence history for a test case of $\theta_{0.7} = 8^o, M_{tip} = 0.612$.

Figure 9 shows blade sectional surface pressure coefficients at two spanwise locations for the hovering rotor at $\theta_{0.7} = 8^o$ and $M_{tip} = 0.612$. In this figure, the computed blade surface pressure coefficients for the 3.6×10^6 and 9.6×10^6 mesh points were compared with the experimental data. The results show that the computed surface pressure coefficients are in good agreement with the experimental data. Note that the use of the fine and coarse meshes did not substantially influence the prediction of the blade surface pressure.

The overall performance of the hovering Caradonna and Tung rotors of different blade solidities, for the test case of $\theta_{0.7} = 8^o$ and $M_{tip} = 0.433$ is shown in Figures 10(a) - (c). From the performance plots, it can be seen that at the same blade collective setting, higher rotor thrust and less rotor torque result from the high aspect ratio blade. The

efficiency of the hovering rotor usually reported as the Figure of Merit (FM). FM measures the ratio of the hovering induced power to the total power required by the rotor to hover. The comparison of the predicted and measured FM versus the C_T/σ is plotted in Figures 10(c). For the high aspect ratio blade, the predicted FM is slightly below the measured data for collective pitch of 5° and 8°.
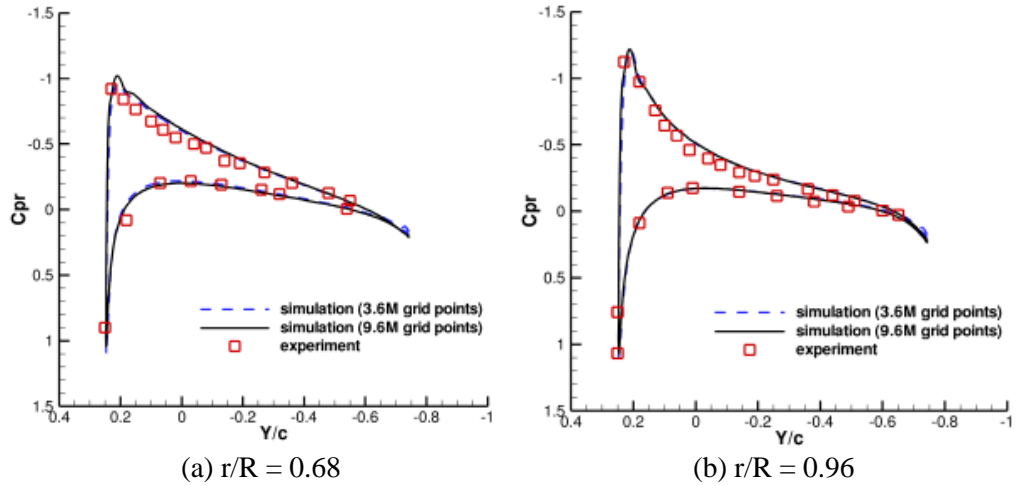

(a) r/R = 0.68   (b) r/R = 0.96

Figure 9 : Comparison of computational and experimental blade surface pressure coefficients for the test case of $\theta_{0.7} = 8^o, M_{tip} = 0.612$.

(a) C_T/σ vs $\theta_{0.75}$ (b) C_Q/σ vs C_T/σ

(c) FM vs C_T/σ
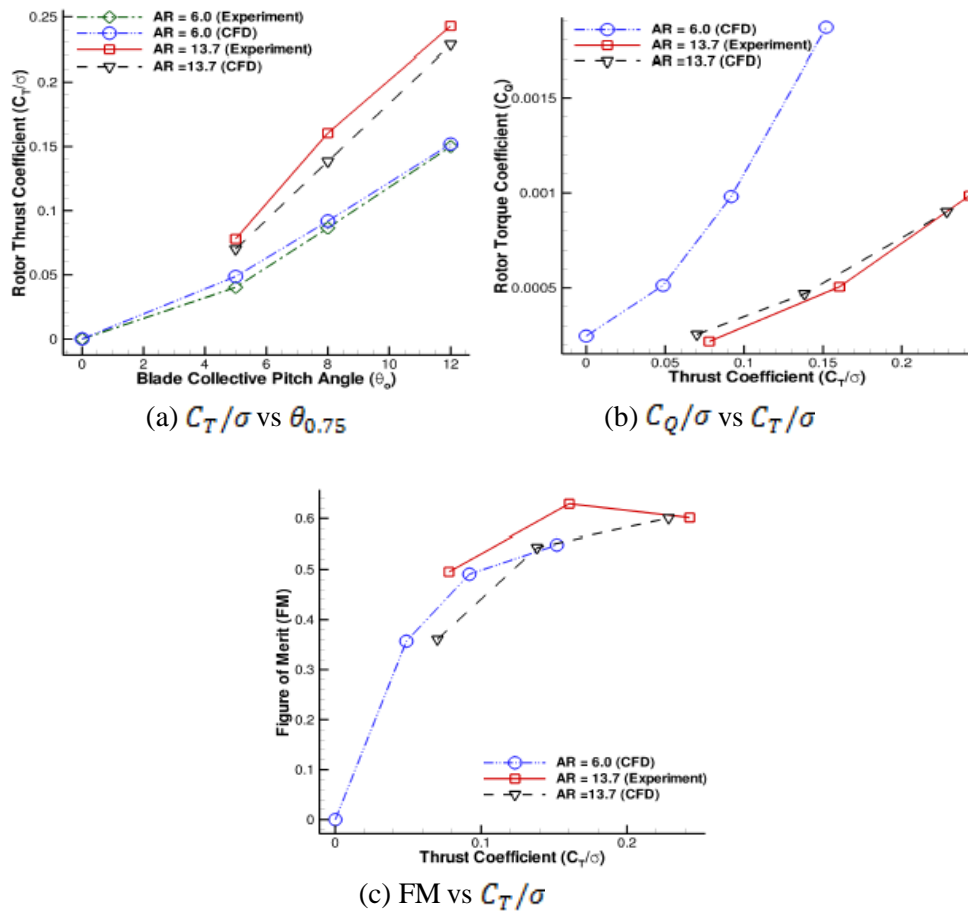
Figure 10 : Performance polar of the Caradonna et.al. model rotors in hover at $M_{tip} = 0.433$.

For C_T/σ between 0.05 and 0.1, a high blade collective pitch is required by the low aspect ratio blade to reach almost the same FM as the high aspect ratio blade. The overall predicted rotor performance is in fair agreement with the experimental data even for the relatively coarse mesh used here.

The computed spanwise distributions of the lift coefficient, C_l for $M_{tip} = 0.439$ and $M_{tip} = 0.612$ are compared with the experimental data and presented in Figures 11(a) and (b). The experimental data is plotted by two different lines to show the differences in the value obtained from the Caradonna and Tung experimental report[12]. In the experimental test, the spanwise distribution of the blade lift coefficients were obtained by integration of the sectional blade surface pressure and presented in tabular format, and as plots of C_l. In this current work, the predicted data are found to be in good agreement with the measured lift obtained from the C_l plots in Ref.12 The radial and vertical tip vortex trajectories extracted based on the vorticity magnitude are presented in Figure 11(c) and (d). The plot shows that the radial and vertical wake trajectory is not substantially influenced by the rotor tip speed. Overall the computed wake geometries are in excellent agreement and consistent with the experimental measurements.

(a) $M_{tip} = 0.433$

(b) $M_{tip} = 0.612$

(c) Axial trajectory

(d) Vertical trajectory
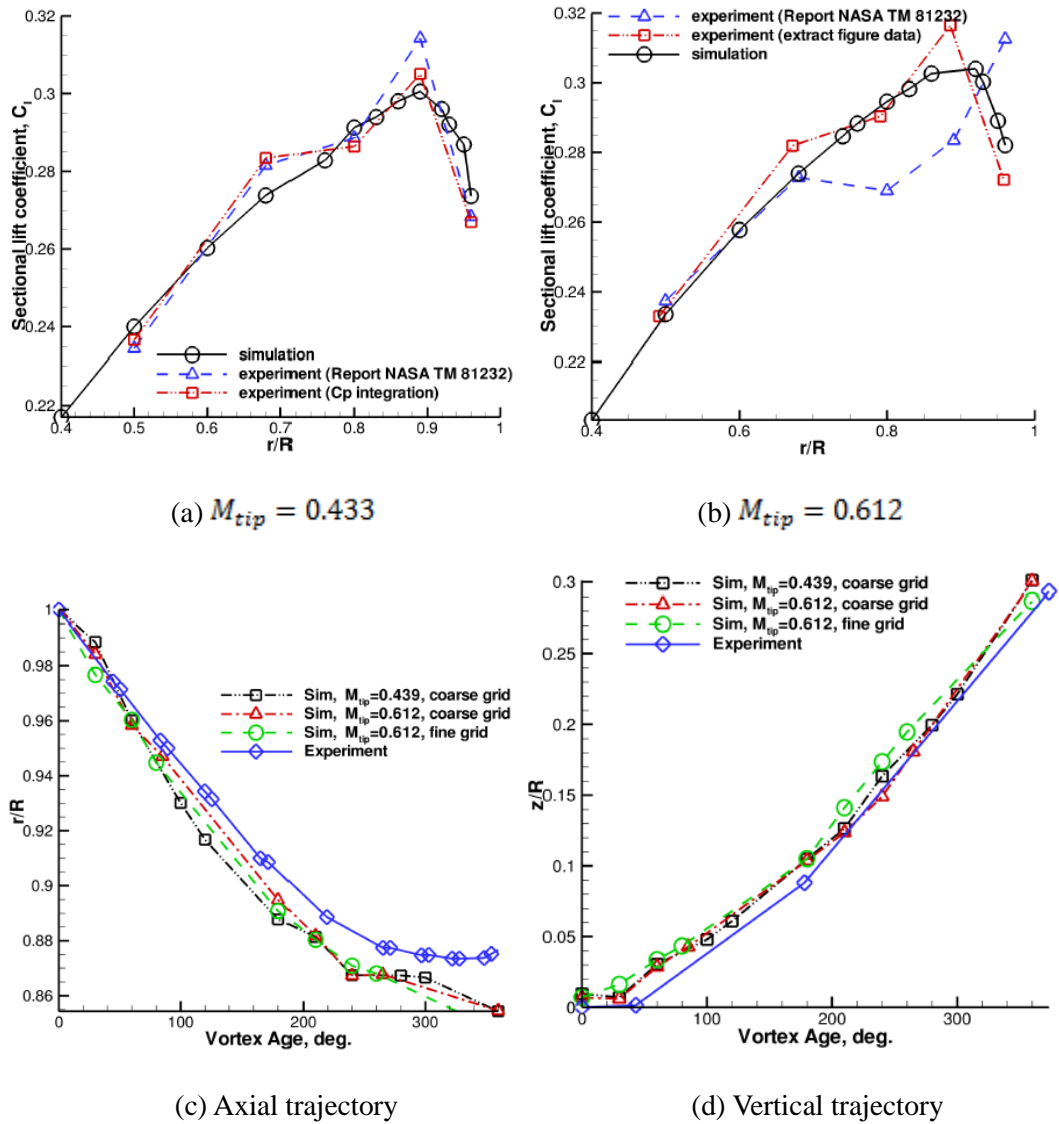
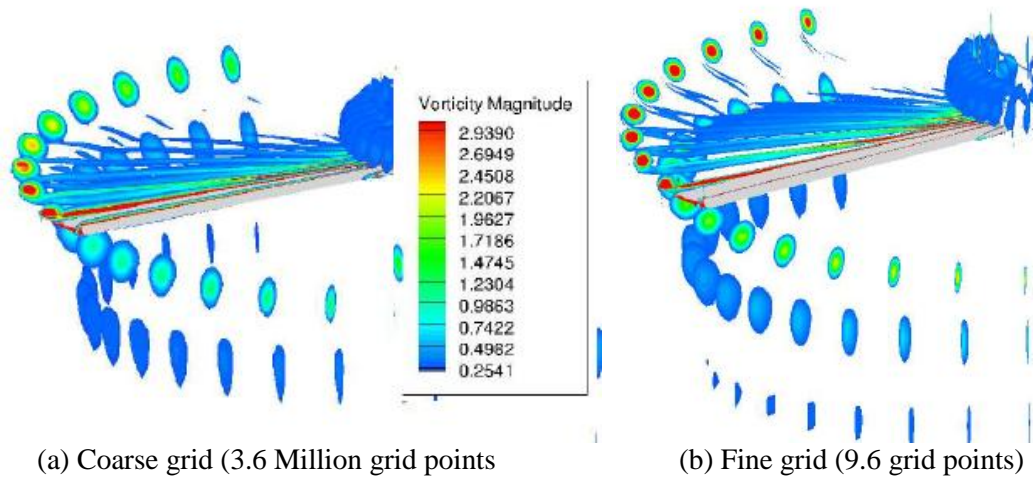Figure 11 : Comparison of blade surface pressure coefficients and wake trajectory for the test case of $\theta_{0.7} = 8^{o}$.

(a) Coarse grid (3.6 Million grid points   (b) Fine grid (9.6 grid points)

Figure 12 : Wake structure of the Caradonna and Tung model rotor in hover
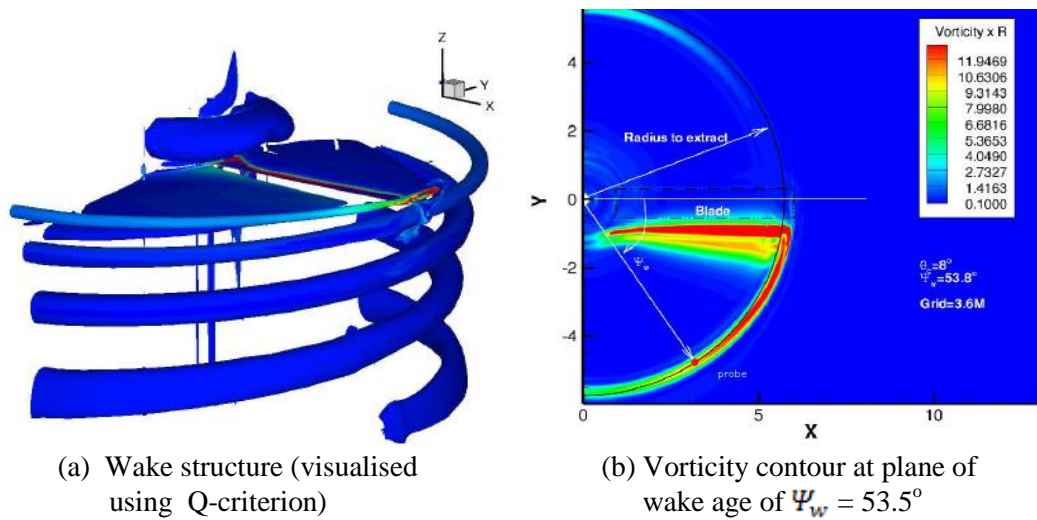($\theta_{0.7} = 8^o$, $M_{tip} = 0.612$).

(a) Wake structure (visualised
     using Q-criterion)
                       (b) Vorticity contour at plane of
                          wake age of $\Psi_w = 53.5^o$

Figure 13 : Wake visualisation of a hovering rotor for the test case of $\theta_{0.7} = 8^o$,
$M_{tip} = 0.612$.

The details of the hovering, Caradonna and Tung rotor tip vortices obtained from the HMB simulation for the coarse and fine mesh resolutions are shown in Figure 12. The tip vortices are extracted every 10 degrees of azimuth. Note that the tip vortices from the coarse mesh diffuse in as early as 3 rotor revolutions, while the tip vortices can still be visualised for up to 5 rotor revolutions in the fine mesh domain.

Furthermore, the details of the wake structure can be visualised by plotting the rotation-dominated strain in the flow using the Q-criterion. Figure 13(a) shows the wake structure of the low aspect ratio rotor in hover for test case of $\theta_{0.7} = 8^o$ and $M_{tip} = 0.612$ as obtained from the fine mesh, and coloured by vorticity magnitude. It can be seen that the radius of tip vortices grows in size at every wake age. As expected, the fine mesh is required to alleviate some of the unwanted dissipation of the coarse mesh.

Another quantity that was extracted is the wake strength. In the current analyses, the wake strengths are extracted as the wake vorticity and pressure time-traces at the location indicated by Caradonna and Tung [12]. The variation of vorticity magnitude and pressure carried by the hovering rotor wake of $\Psi_w = 59.5^o$ extracted at various azimuth angles are presented in Figures 14(a) and (b) respectively. The peaks are found to be

contributed from the blade passage, vortex sheet and vortex-probe interactions. For the vorticity time trace, the highest vorticity magnitudes are found to be contributed by the vortex-probe interaction whereas the contribution from the vortex sheet is also important. A small peak was contributed from the blade passage over the probe. For the pressure time-trace, the highest pressure peaks are captured by the blade passing over the probe (Figure 14b). The computed wake strength and pressure from the second blade has shown a similar pattern as from the first blade. In terms of the wake trace pattern, the computed wake trace seems to agree, qualitatively, with the experimental data. Unfortunately, further comparisons were not possible since the work of Caradonna and Tung [12] provided very detailed blade loads but fewer data is available for the wake.

6.3   Results of Vortex Core Diffusion

The details of the computed tip vortex core modelled using the Vatistas model are analysed and plotted in Figure 15. For the analytical model, a 2D Cartesian mesh was generated to evaluate the Vatistas vortex model with different diffusion parameters, *n*. Figure 15(a) shows the mesh system used to model the Vatistas vortex profile. The computational domain had a square geometry of 10×10 unit lengths in the *x*- and *y*-directions. The domain was discretised using 71×71 mesh points

(a) Vorticity time-trace   (b) Pressure time-trace
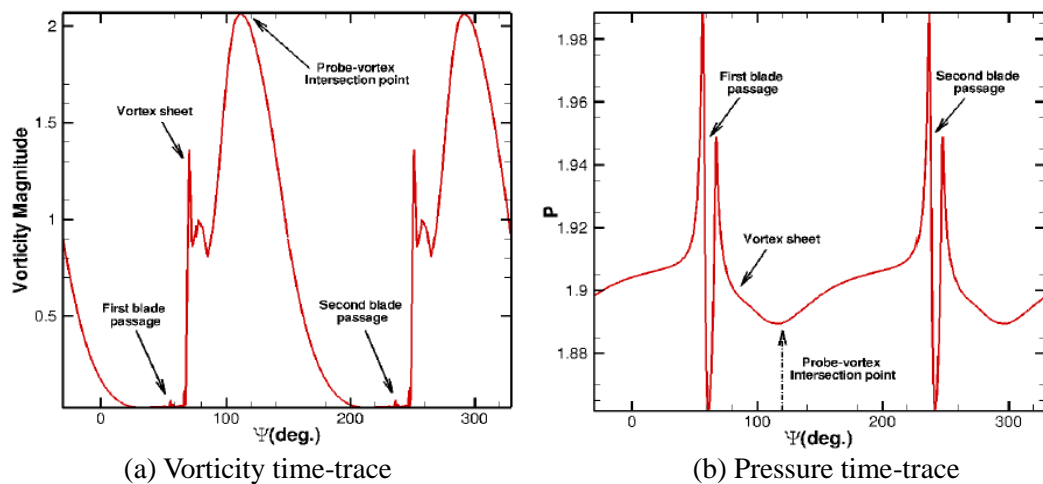
Figure 14 :   Wake vorticity magnitude and pressure-time trace at $\theta_{0.7} = 8^o$, $M_{tip} = 0.612$ and vortex age, $\Psi_w = 59.5^o$

and contained about 21 points across the vortex core diameter in the vertical and horizontal directions. In the Vatistas model, the vortex core was positioned at the centre of the domain as shown in Figure 15(a). For comparison, the number of mesh points across the vortex core in the Vatistas model should be identical to the mesh generated for CFD. In this test case, both meshes have about 20 points across the vortex core.

For the Vatistas analysis, the information about the vortex core radius and circulation were obtained from the HMB2 simulations. For the coarse and the fine meshes, the vortex core radii were extracted at a wake age of, $\Psi_w = 180^o$ were $r_c = 0.2625c$ and $r_c = 0.1935c$ respectively. The circulation (Γ) around a vortex core obtained from the HMB2 simulation was calculated and found that the circulation around the vortex core was 0.1195 rad/s for the coarse and 0.1283 rad/s for the fine mesh, respectively. Using these data, the Vatistas vortex model was generated as shown in Figure 15(a) for a low diffusive parameter of $n = 3$. The comparison of the vortex core properties (vorticity magnitude and induced axial velocity) obtained from CFD simulations and the analytical results of Vatistas vortex model for different diffusive parameters are shown in Figure 15(c) to (f). Referring to Figures 15(c) and (d), the

Vatistas vortex model with a diffusive parameter greater than one is less diffusive and has high vorticity concentration at the centre of vortex core. Figures 15(e) and (f) show the distribution of the axial induced velocity components for the coarse and fine HMB2 meshes. From the comparison, it is suggested that the diffusive ($n = 1$) Vatistas vortex model is well suited to model the rotor vortices base on the employed CFD mesh used. The comparison shows that although blade loads and wake geometry are adequately resolved, the vortex core still require mesh refinement.

(a) Closed-up view of Vatistas vortex core (n = 3)

(b) Tip vortex core of lifting rotor in hover ($M_{tip} = 0.612$, $\Psi_w = 180^o$)

(c) Profile of vorticity magnitude (Coarse grid)

(d) Profile of vorticity magnitude (Fine grid)

(e) Profile for axial induced velocity

(f) Profile for axial induced velocity
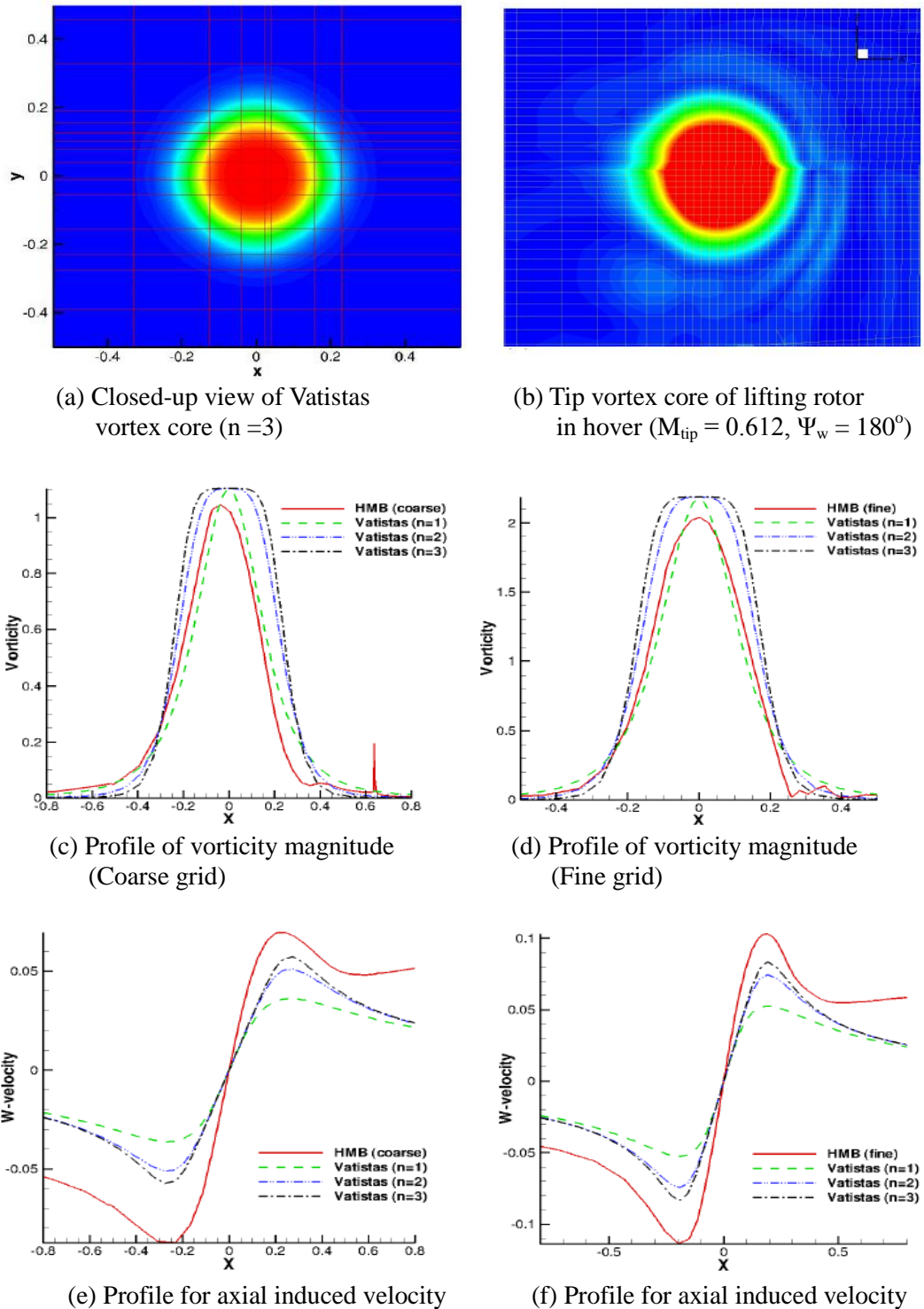
Figure 15 : Vatistas model and CFD results for the properties of the tip vortex core.

6.4   Results of Different Far-field Models on Hovering Rotors

The results discussed so far were obtained from the modified Srinivasan far-field boundary condition which is currently used in the HMB2 solver. The flowfields and blade loads of the ONERA 7AD1 and Caradonna and Tung model rotor in hover have also been modelled using the source-sink boundary condition of Srinivasan8 and the new far-field boundary conditions based on the vortex tube models.[9] To test these far-field boundary conditions, inviscid and viscous flow computations of hovering rotors have been conducted. For the inviscid flow computation, the 7AD1 rotor model is used and the Caradonna and Tung model rotors are used for the viscous computations. The mesh geometry of the 7AD1 rotor generated contained approximately 1.7 Million mesh points and was divided in 142 blocks. The coarseness of the grid for the 7AD1 rotor, however, did not allow for detailed wake resolution. The comparison of the sectional blade surface pressure coefficients of the 7AD1 rotor in hover modelled using different far-field boundary conditions are plotted in Figure 16. From the C_p plot, the use of different far-field boundary conditions had a very small effect on the blade surface pressure coefficients.

(a) r/R = 0.50   (b) r/R = 0.70

(c) r/R = 0.915   (d) r/R = 0.975
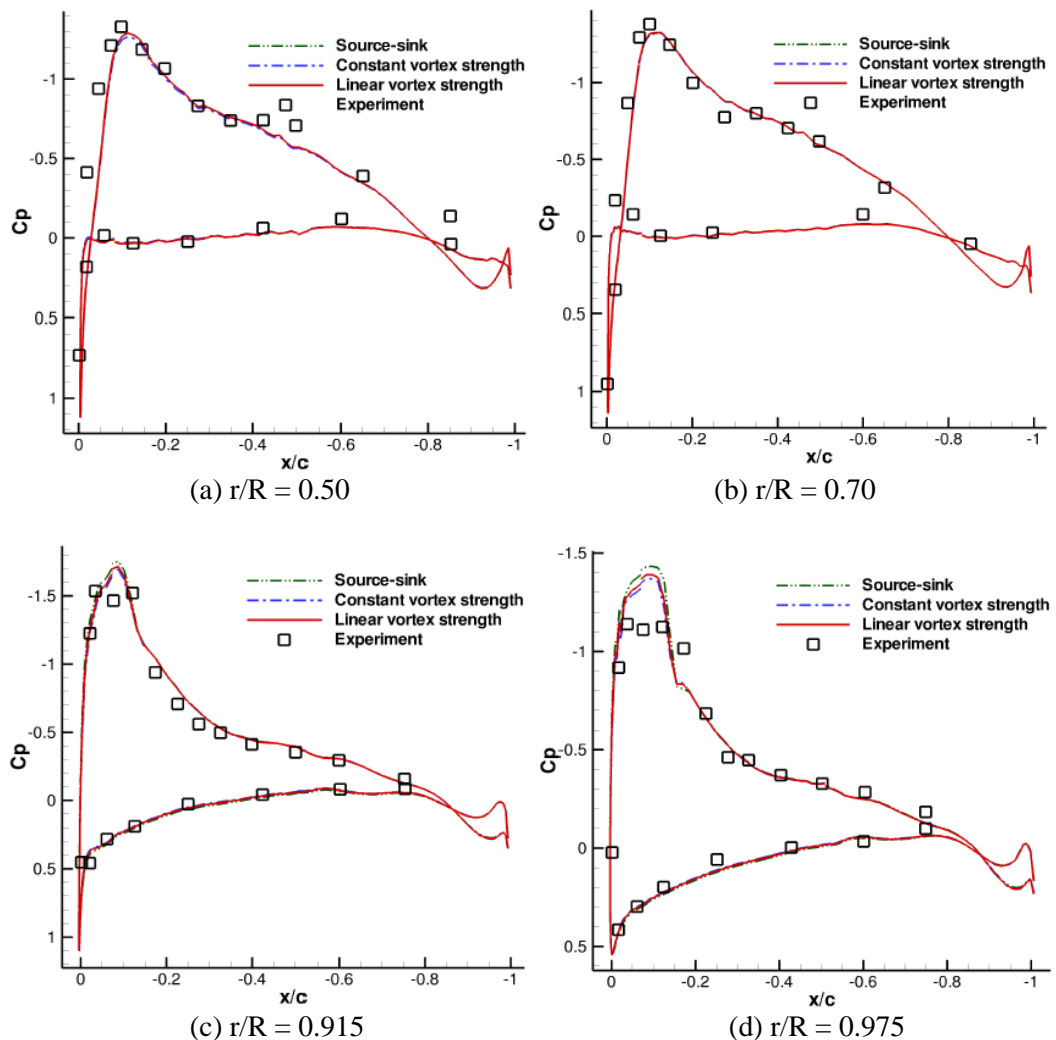
Figure 16 :   Comparison of The 7AD1 rotor blade surface pressure coefficient for different far-field boundary conditions $\theta_{0.7} = 7.5^o$, $M_{tip} = 0.6612$.

Further investigations of the 7AD1 rotor were performed for different distances of the outflow boundary from the rotor disk. These tests performed to investigate the effect of the flowfield, blade loads, and solution convergence of the Srinivasan (Model 1) far-field boundary model with different sizes of computational domains (shown in Figure 18). The grid points are kept the same in all test cases, so shortening the distance of outflow boundary to the rotor disk plane improves the grid resolution below the rotor plane.

Figure 17 shows the effect of the different outflow distances on the blade pressure distribution and wake displacement of the ONERA 7AD1 rotor in hover. The blade C_p, seems not to be influenced by the used of different domain size. However, the streamlines of the secondary flowfield show a different picture (Figure 18). Using the Model 1 far-field boundary condition, the recirculation flow developed below the rotor plane does not leave the outflow boundary as it changes in size to a shorter and wider. The comparisons of the tip vortices displacements are also compared. Table 3 shows the effect of shorter computational domain on the rotor thrust, torque and figure of merit.

Overall, using the Model 1 of the source-sink boundary and reducing the rotor outflow boundary distance below the rotor disk, shows a slightly increasing in rotor thrust and torque coefficients to hover. This result however, shows a decrease in the rotor hovering efficiency represented by the figure of merit compared to the results obtained from the full domain simulation.

The effect of the different far-field boundary conditions on the blade surface pressure coefficients of the hovering low aspect ratio Caradonna and Tung model rotor are shown in Figure 19. Overall, the blade C_p is not affected much by the far-field boundary used and a very slightly different of C_p can be seen near the suction region of the blade. The comparisons of the spanwise blade lift coefficient and the tip vortex trajectories are plotted in Figures 20(a) and (b). The lift plot seems more sensitive and fairly agrees with experimental results. Despite this result, generally good agreement is seen between the experimental and computational vortex trajectories.

Table 3:   The effect of domain outflow distance on the hovering ONERA 7AD1 rotor thrust coefficient, torque coefficient and the figure of merit

Case	Full domain	30 % shorter outflow	Δ (%)	50 % shorter outflow	Δ (%)
C_T	1.30554e-02	1.36364e-02	4.45	1.36264e-02	4.37
C_Q	8.65654e-04	9.50604e-04	9.81	9.47774e-04	9.49
FM	8.61609e-01	8.37570e-01	-2.79	8.39148e-01	-2.61

Figure 21 shows the comparison of the normalised velocity distribution taken at the plane of rotor disk and at the outflow boundary of the computational domain. At the plane of rotor disk, the distribution of *U, V*, and *W*-velocities are almost identical for all far-field boundaries tested. At the outflow boundary, the magnitude of velocity fields observed however varies with the far-field boundary models used. As shown in Figure 21(f), both vortex-tube models produce almost the same magnitudes of velocity at the outflow boundary but less than the source-sink boundary models.

(a) r/R = 0.50
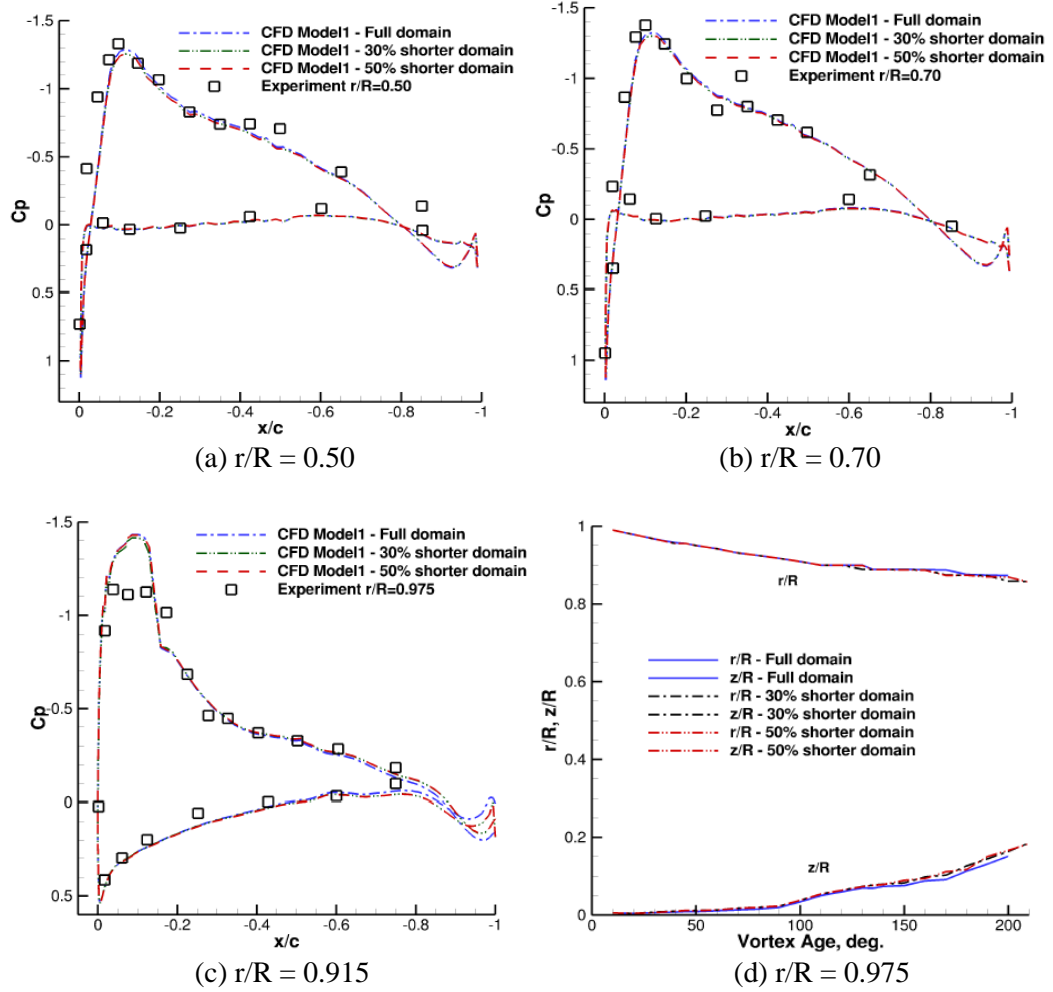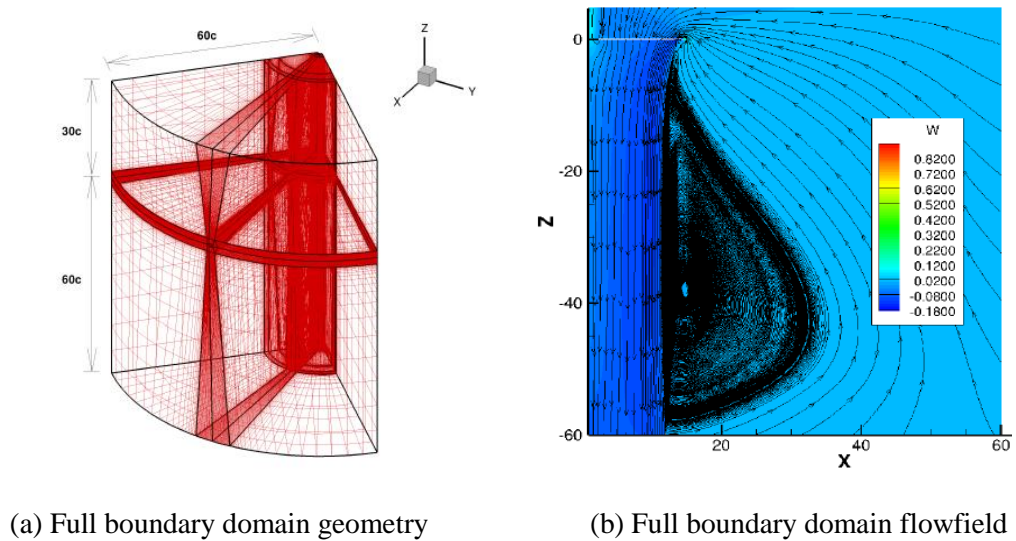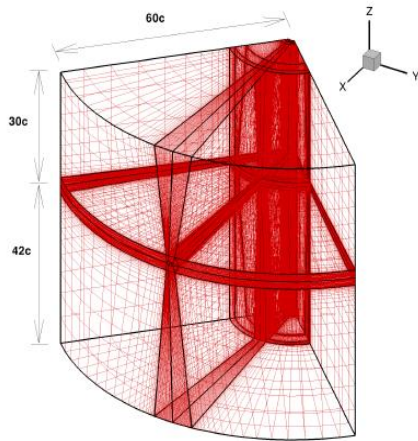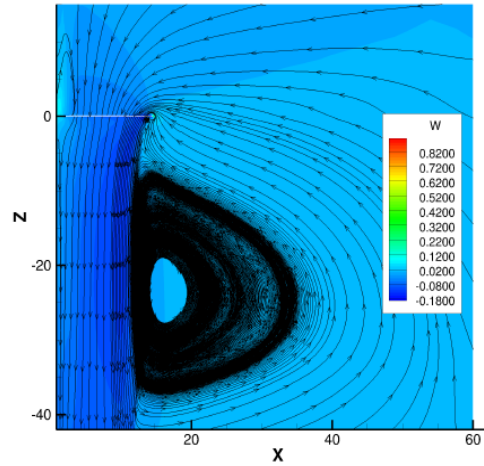
(b) r/R = 0.70

(c) r/R = 0.915

(d) r/R = 0.975

Figure 17 : Comparison of hovering 7AD1 rotor blade surface pressure coefficient and tip vortex trajectory modelled using modified Srinivasan far-field boundary condition and different CFD domain size ($\theta_{0.7} = 7.5^o$, $M_{tip} = 0.6612$).
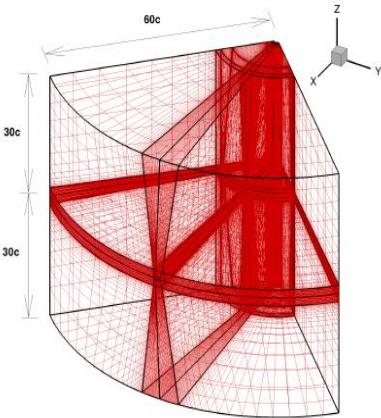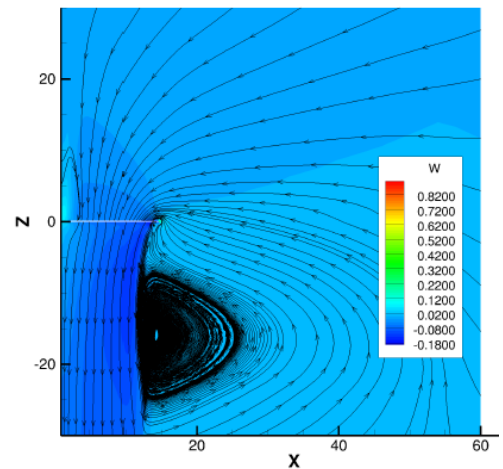

(a) Full boundary domain geometry

(b) Full boundary domain flowfield

(c) 30% shorter outflow domain geometry

(d) 30% shorter outflow domain flowfield

(e) 50% shorter outflow domain geometry

(f) 50% shorter outflow domain flowfield

Figure 18 : Comparison of computational domain size and its flowfields pattern for the ONERA 7AD1 rotor in hover modelled using Model 1 (modified Srinivasan) far-field boundary condition ($\theta_{0.7} = 7.5^{o}$, $M_{tip} = 0.6612$)
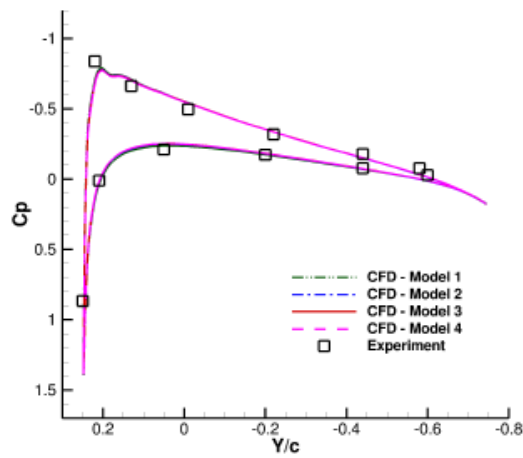
(a) r/R = 0.50
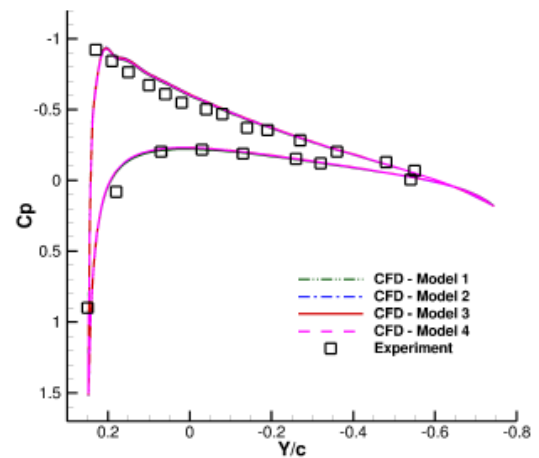
(b) r/R = 0.68

(c) r/R = 0.50   (d) r/R = 0.68
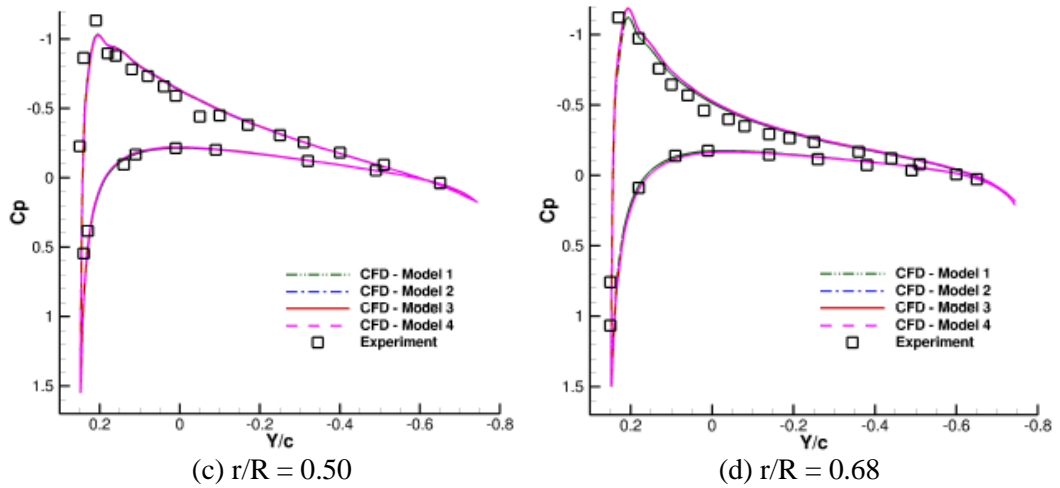
Figure 19 : Comparison of The Caradonna and Tung blade surface coefficient for different far – field boundary conditions ($\theta_{0.7} = 8^o$, $M_{tip} = 0.612$)

(a) Sectional lift coefficient   (b) Wake trajectory
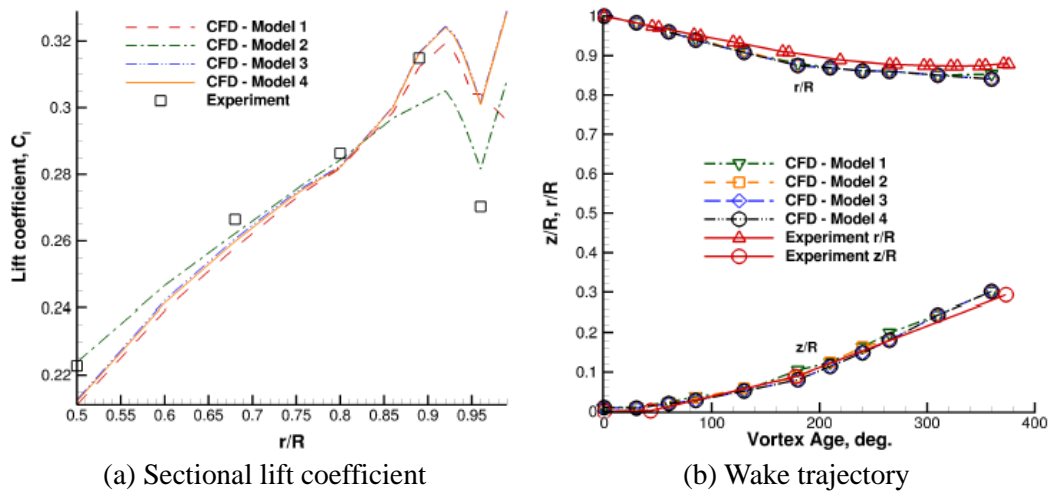
Figure 20 : Comparison of the Caradonna and Tung sectional blade lift coefficient and wake trajectory for different far-field boundary conditions ($\theta_{0.7} = 8^o$, $M_{tip} = 0.612$)
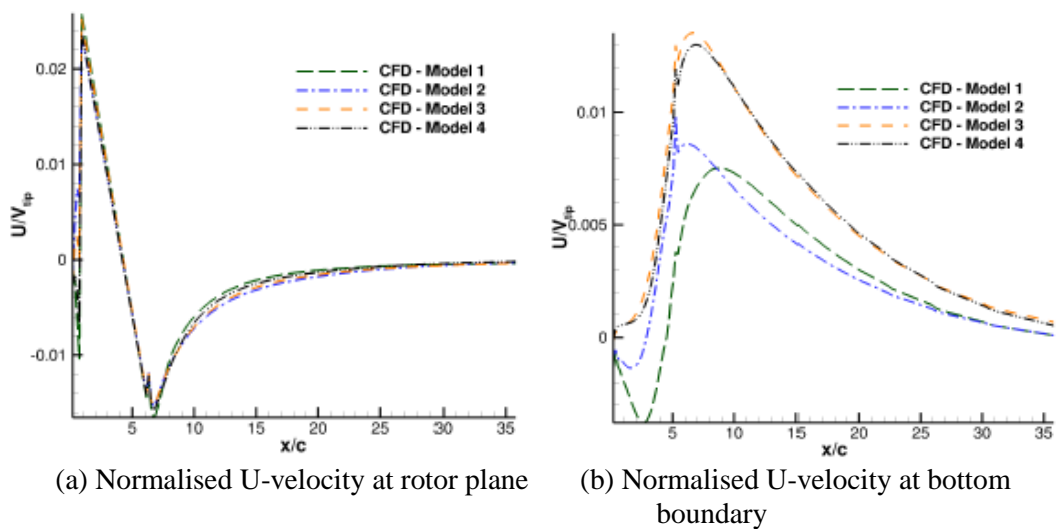
(a) Normalised U-velocity at rotor plane   (b) Normalised U-velocity at bottom boundary

(c) Normalised V-velocity at rotor plane

(d) Normalised V-velocity at bottom boundary

(c) Normalised W-velocity at rotor plane

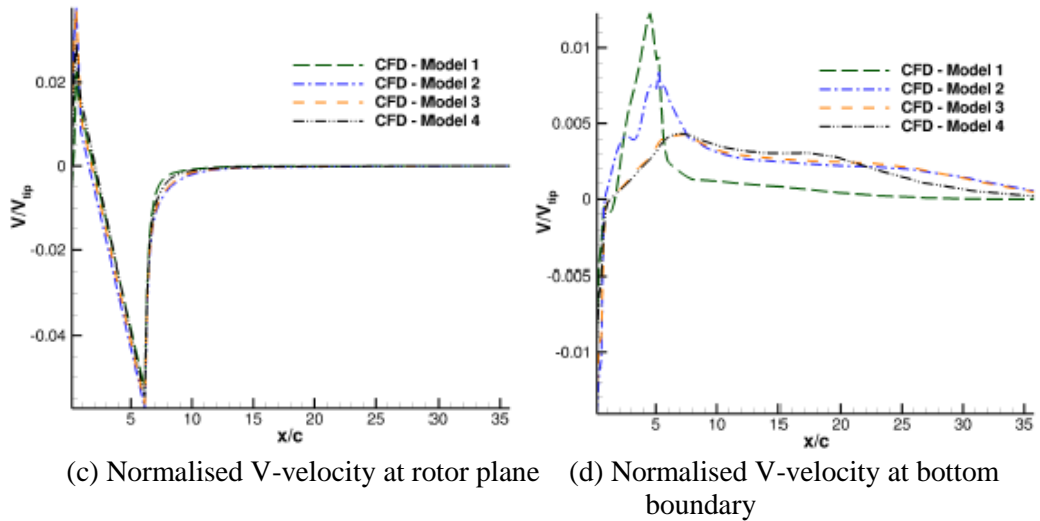(d) Normalised W-velocity at bottom boundary
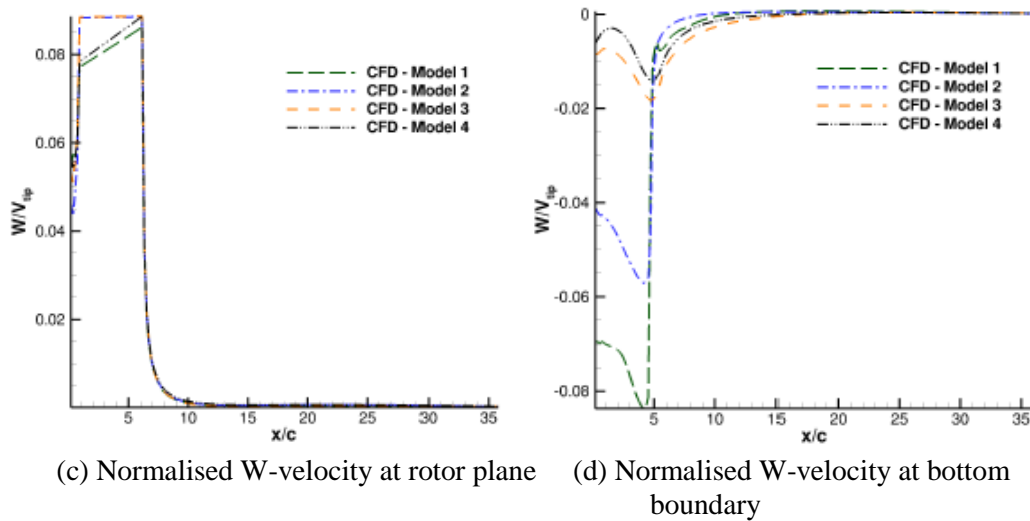
Figure 21 : Comparison of the Caradonna and Tung rotor velocity distribution taken at rotor plane and bottom domain boundary for different far-field boundary conditions ($\theta_{0.7} = 8^{o}$, $M_{tip} = 0.612$)

6.5 Results for The Climbing Caradonna UH-1H Model Rotor

In climbing test cases, the vertical climb speed of the rotor has been included in the source-sink predictions of the flow velocity at far-field boundary. This resulting the increment in the overall flow speed that moves downstream the outflow boundary. Results for the Caradonna UH-1H model rotor performance and tip vortex trajectory prediction are now presented. The results were obtained using the modified source-sink far-field boundary (Model 1)[16] and tested for a range of climbing rates from 0 to 0.04. For this test case, the calculations were performed for a blade collective pitch angle, $\theta_{o} = 11^{o}$, tip Mach number, $M_{tip} = 0.5771$ and Reynolds number, $Re = 1.028 \times 10^{6}$. The rotor climbing rate which was normalised with the blade tip speed was the only variable altered.
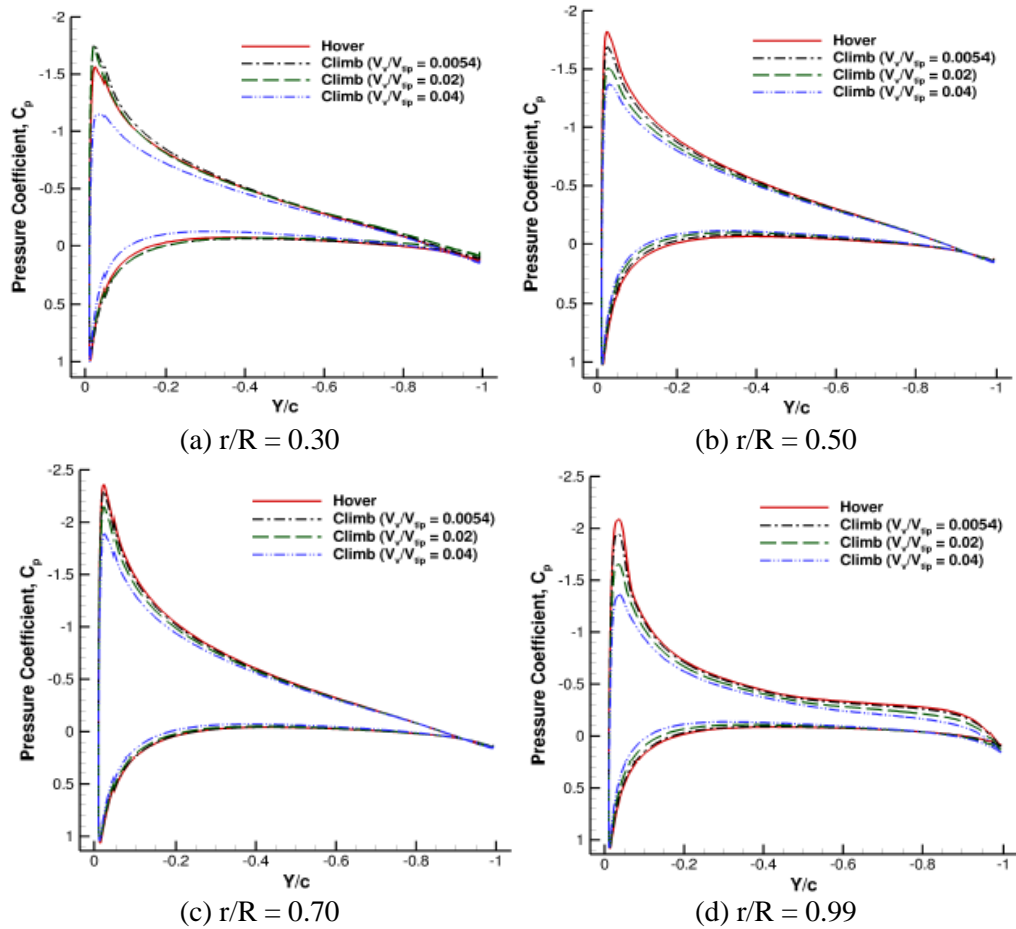
(a) r/R = 0.30   (b) r/R = 0.50

(c) r/R = 0.70   (d) r/R = 0.99

Figure 22 :   Comparison of CFD results of the Caradonna UH-1H blade surface pressure coefficients at different rates of climb ($\theta_{0.7} = 11^{o}$, $M_{tip} = 0.5771$)

The effect of the trimming on the rotor performance and wake displacement was also carried-out. In the trimmed conditions, the thrust required for climb was maintained closed to the hover state. This is done by considering the incremental of the blade collective pitch settings by $3/4 V_c/V_{tip}$ while the coning angle was set to zero for all calculation performed [23]. For the climbing test cases considered, the linear increment in the blade collective pitch resulting from the trimmed conditions are plotted in Figure 23(a). Figure 23(c) shows that a higher rotor torque is required for trimmed conditions, and a slightly increase in the figure of merit is observed.
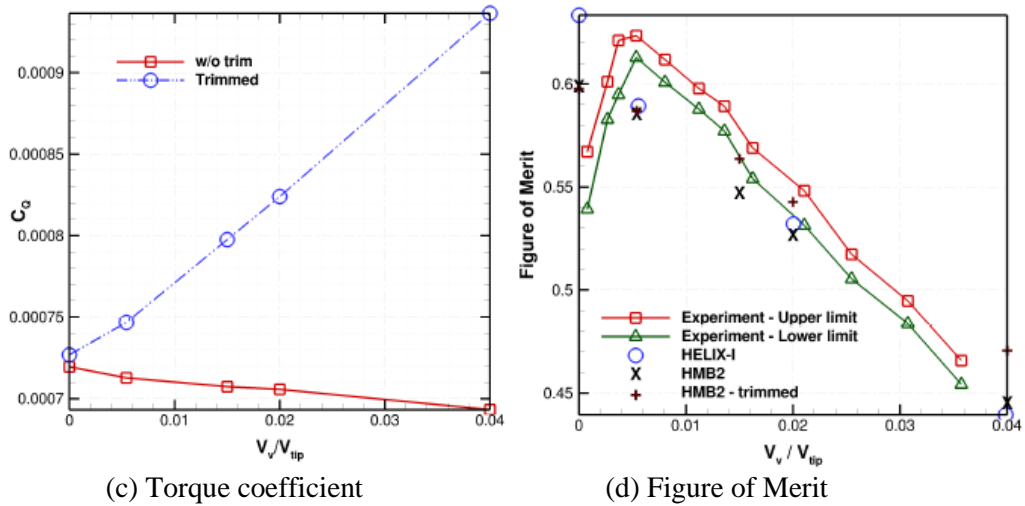

(a) Collective pitch   (b) Thrust coefficient

(c) Torque coefficient   (d) Figure of Merit
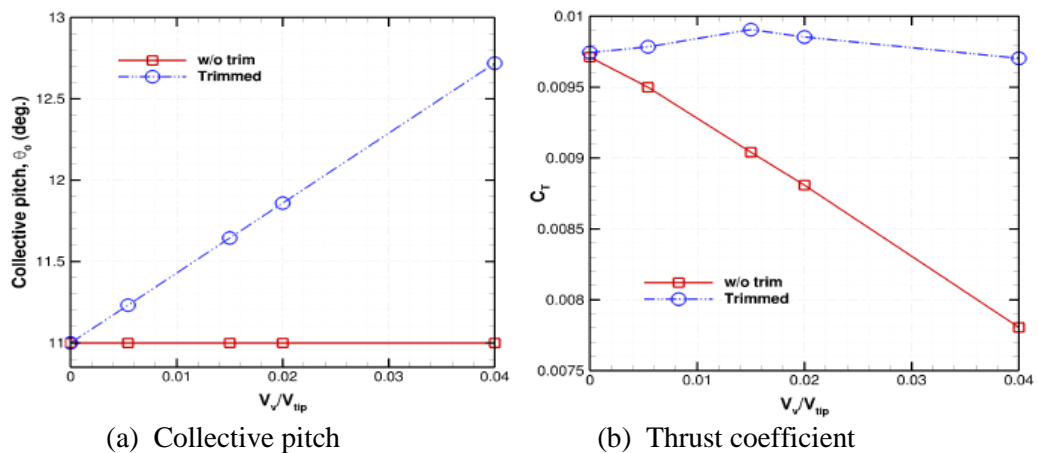
Figure 23 : The performance of the Caradonna UH-1H rotor in hover and vertical climb ($\theta_{0.7} = 11^o$, $M_{tip} = 0.5771$)

In addition, the prediction of the rotor figure of merit using the HMB2 CFD solver for rotor without trimmed condition is slightly below the experimental results for all test cases but in good agreement with HELIX-I data for climbing cases. In the low speed region and hover conditions, Caradonna explained in his report that the value of the figure of merit in this region had dropped due to excessive flow unsteadiness [15]. Thus the extrapolation to the linear climb was used to estimate the hover figure of merit. The predicted hover figure of merit using HMB2 shows a linear trend, however, the value of the figure of merit falls between experiment and the HELIX-I data. Trimming the rotor collective pitch increases the rotor figure of merit in the fast climb cases (Figure 23(d)).

Figure 24(a) shows the spanwise blade lift coefficients for different rotor climbing rate. It is apparent that, the spanwise lift coefficient is shifted vertically downwards as the normalized climbing velocity increases from hover to 0.04. For the typical test case, a slightly incremental in the spanwise blade loading can be seen resulting from the trimming condition (Figure 24(b)).
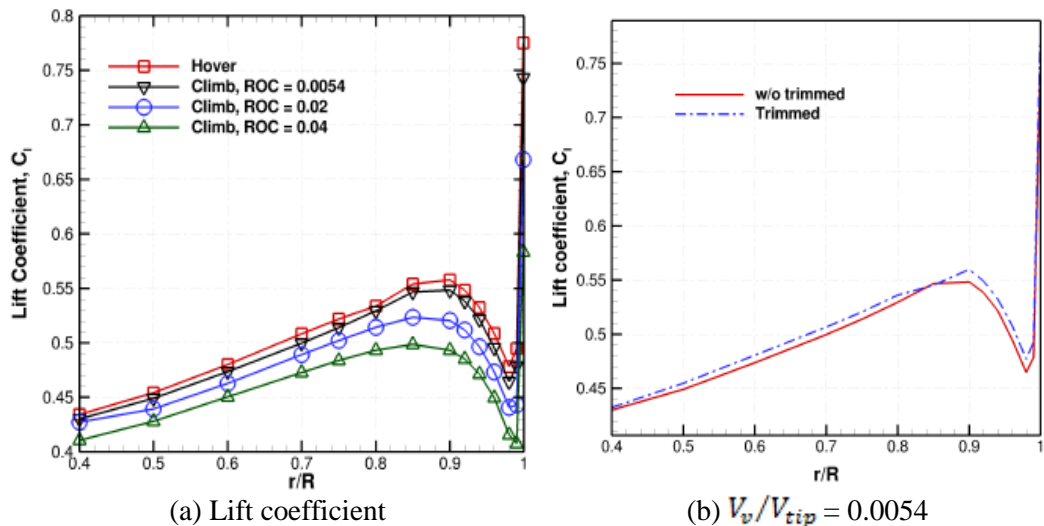

(a) Lift coefficient   (b) $V_v/V_{tip} = 0.0054$

Figure 24 : The distribution of spanwise blade lift coefficients at different rotor climb rates ($\theta_{0.7} = 11^o$, $M_{tip} = 0.5771$)
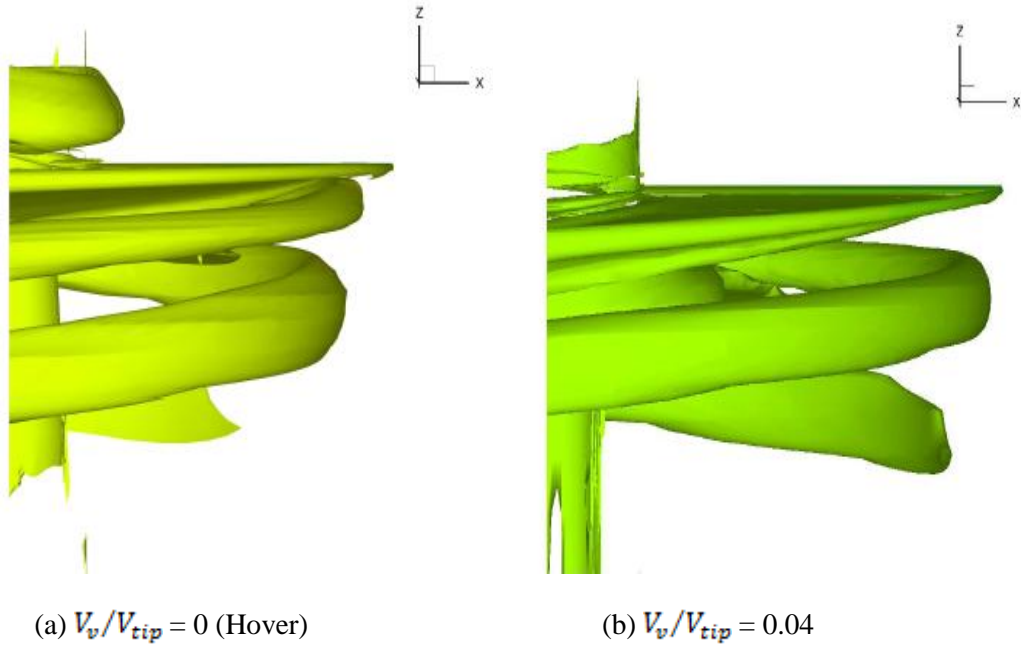
(a) $V_v/V_{tip} = 0$ (Hover)   (b) $V_v/V_{tip} = 0.04$

Figure 25 : Wake structures of climbing rotor visualised using Q-criterion (coloured by pressure) for test case of $\theta_{0.7} = 11^o$, $M_{tip} = 0.5771$.

Figure 26(a) to (d) show the comparison of the rotor tip vortex trajectory for different rotor vertical speed settings. It can be seen that the calculated wake trajectories are in good agreement with the experimental data of blade number 1[15]. As shown in Figure 26(d), the rotor tip vortices show more contraction in hover than in climbing flight, and the tip vortices descending faster in climbing cases. It can be seen that the wake geometry does not change in trimmed condition. The details of the rotor wake geometry visualized using Q-criterion are depicted in Figure 25(a) and (b). The figures show that the step of wake spirals is proportional to the climbing ratio. For the case of $V_v/V_{tip} = 0.04$, the vortices are displaced almost twice as for the rotor disk in comparison to hover.

(a) Hover   (b) $V_v/V_{tip} = 0.0054$
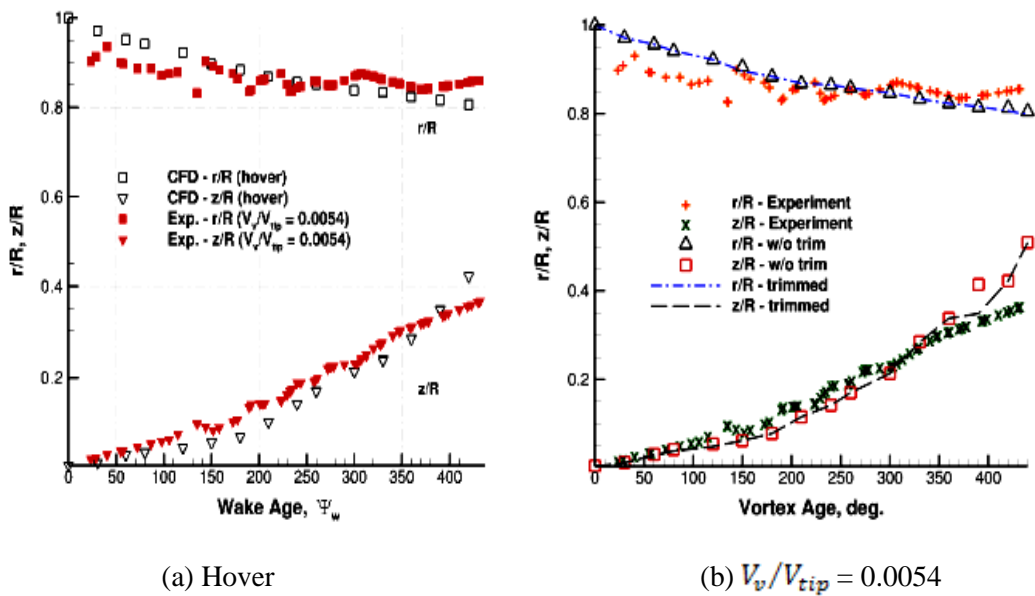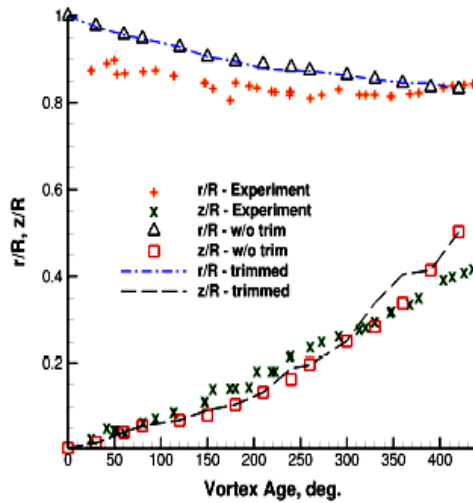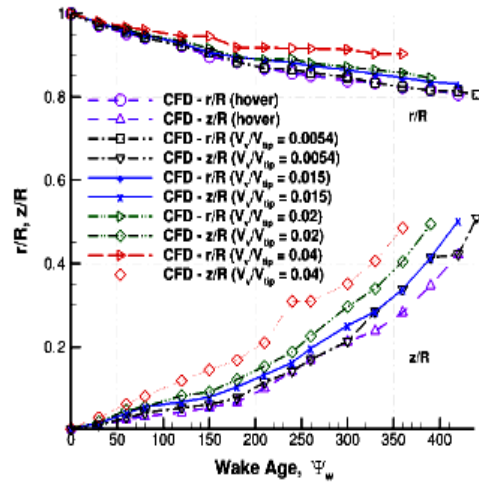
(c) $V_v/V_{tip} = 0.015$ (d) Comparison

Figure 26 :   Tip vortex geometry of rotor in different climb rates ($\theta_{0.7} = 11^o$, M_{tip}= 0.5771).

7.0   CONCLUSIONS

This research studied the effect of different far-field boundary models on the hovering and climbing model helicopter rotors. The study began by modelling the far-field boundary using a simple momentum theory and then simulated using a RANS CFD methods. From the initial study using simple momentum theory, reasonable flowfield patterns closed to real rotor flow were observed by the vortex tube model with linearly reduced vortex strength. The results show that the vortex tube model is a possible option as an initial solution to improve the speed of the CFD analysis.

The Parallel Helicopter Multi-block CFD solver have been used and validated for the Caradonna and Tung model rotor in hover. The blade loads, wake geometry and wake strength were analysed and the effect of the number of mesh points on the blade loads and wake geometry were also investigated. From the simulation, excellent agreement of the blade loads data and wake trajectories between CFD and experiment have been observed for mesh of more than 3.6 and 9 Million points per blade.

The wake time-trace analysis of the Caradonna and Tung rotor showed a periodic nature of the hovering rotor wake taken below the rotor plane (in this case, the rotor wake extracted at wake age of 59.5^o) between the first and the second blade passages. However, a great concern is on the wake diffusion problem due to a poor mesh resolution far from the rotor. A high number of mesh points is required for better wake capturing and prediction. An analytical study of vortex core induced velocity using Vatistas vortex model has also been carried-out. Different diffusive parameters have been used to determine the decay of the tip vortices of the Caradonna and Tung rotor in hover. It was found that grids of about 9 Million per blade were still modelling a diffusive core.

The effects of different far-field boundaries and initial conditions with full and shorter domain outflow distances on the blade surface pressure have also been investigated. The use of different far-field boundaries had little effect on the blade surface pressure coefficients and wake geometry, however sensitivity on the spanwise lift coefficient was observed. The use of a shorter domain outflow influences the flowfield pattern below the rotor plane, and reducing the computational domain resulted in increase of the rotor thrust coefficient and decreased the figure of merit. With the employed solver and mesh density the domain had to be kept to a minimum of 5R below the rotor plane.

For the axial climb test case, the blade figure of merit computed based on the Model 1 far-field boundary shows a linear trend from hover to the climb rate of 0.04. It was also observed that, the rotor tip vortex trajectories were correctly predicted where more contraction in hover and lower climb than at higher climb speed. Overall, the results of the blade loads and tip vortex position are in excellent agreement with the experimental data, suggests that CFD can adequately resolve the loads and wake structure. Further work is however, needed to resolve the details of the vortex cores.

ACKNOWLEDGEMENT

REFERENCES

1. Dietz, M., Kebler, M., Kramer, E., and Wagner, S., "Tip Vortex Conservation on a Helicopter Main Rotor Using Vortex- Adapted Chimera Grids," AIAA Journal , Vol. 45, No. 8, 2007, pp. 2062–2974.
2. Strawn, R. G. and Djomehri, M. J., "Computational Modelling of Hovering rotor and Wake Aerodynamics," Journal of Aircraft , Vol. 39, No. 5, 2002, pp. 786–793.
3. Hariharan, N. and Sankar, L. N., "A Review of Computational Technique or Rotor Wake Modeling," AIAA–00–0114.
4. Boelens, O. J., van der Ven, H., Oskam, B., and Hassan, A. A., "Accurate and Efficient Vortex-Capturing for Rotor Blade Vortex Interaction," NLR-TP-2000-051, 2000.
5. Zhao, J. and He, C., "A Viscous Vortex Particle Model for Rotor Wake and Interference Analysis," American Helicopter Society, 64th Annual , 2008.
6. Zhao, Q. J., Xu, G. H., and Zhao, G. J., "New Hybrid Method for Predicting the Flowfields of Helicopter Rotors," Journal of Aircraft , Vol. 43, 2006, pp. 372–380.
7. Anusonti-Inthra, P. and Floros, M., "Coupled CFD and Particle Vortex Transport Method: Wing Performance and Wake Validations," 38th Fluid Dynamics Conference and Exhibition, AIAA 2008-4177, 2008.
8. Srinivasan, G. R., "A Free-Wake Euler and Navier-Stokes CFD Method and Its Application to Helicopter Rotors Including Dynamic Stall," JAI Associate, Inc 93-01, Nov. 1993.
9. Wang, S. C., "Analytical Approach to the Induced Flow of a Helicopter Rotor in Vertical Descent," Journal of the American Helicopter Society, Vol. 35, 1990, pp. 382–397.
10. Choi, W., Lee, S., Jung, J., and Lee, S., "New Far-Field Boundary and Initial Condition for Computation of Rotors in Vertical Flight Using Vortex Tube Model," Journal of the American Helicopter Society, Vol. 43, 2008, pp. 382–397.
11. Perry, F. J., Chan, W. F. Y., Simon, I., Brown, R. E., Ahlin, G. A., Khelifa, B. M., and Newman, S. M., "Modelling the Mean Flow through a Rotor in Axial Flight Including Vortex Ring Conditions," Journal of the American Helicopter Society, Vol. 52, 2007, pp. 224–238.
12. Caradonna, F. X. and Tung, C., "Experimental and Analytical Studies of a Model Helicopter Rotor in Hover," 1981.
13. Tung, C., Pucci, S. L., Caradonna, F. X., and Morse, H. A., "The Structure of Trailing Vortices Generated by Model Rotor Blades," Nasa tm 81316, 1981.

14. Ramasamy, M., Johnson, B., Huismann, T., and Leishman, J. G., "Procedures for Measuring the Turbulence Character- istics of Rotor Blades Tip Vortices," Journal of the American Helicopter Society, Vol. 54, 2009, pp. 1–17.

15. Caradonna, F. X., "Performance Measurement and Wake Characteristics of a Model Rotor in Axial Flight," Journal of the American Helicopter Society, 1999, pp. 101–108.

16. Steijl, R., Barakos, G., and Badcock, K., "A Framework for CFD Analysis of Helicopter Rotors in Hover and Forward Flight," International Journal for Numerical Methods in Fluids, Vol. 51, 2006, pp. 819–828. doi: 10.1002/fld.1086.

17. Brocklehurst, A., Steijl, R., and Barakos, G., "CFD for Tail Rotor Design and Evaluation," 34th European Rotorcraft Forum, 2008.

18. Choi, W., Lee, S., Jung, J., and Lee, S., "Numerical Prediction of Hovering Rotor Tip Vortex using Vortex Tube Model Boundary Condition," The European Rotorcraft Forum, 2007.

19. Castles, W. J. and Gray, R. B., "Empirical relation between induced velocity, thrust, and rate of descent of a helicopter rotor as determined by wind-tunnel tests on four model rotors," NACA TN 2474, 1951.

20. Badcock, K. J., Richard, B. E., and Woodgate, M. A., "Elements of Computational Fluid Dynamics on Block Structured Grids using Implicit Solvers," Progress in Aerospace Sciences, Vol. 36, 2000, pp. 355–364.

21. Wilcox, D. C., "Reassessment of the Scale Determining Equation for Advanced Turbulence Models," AIAA Journal , Vol. 25, 1988, pp. 1299–1310.

22. Gagliardi, A. and Barakos, G. N., "Improving Hover Performance of Low-Twist Rotors using Trailing-Edge Flaps - A Computational study," 34th European Rotorcraft Forum, 2008.

23. Johnson, W., Helicopter Theory, Princeton University Press, 1980.

24. Vatistas, G. H., Kozel, V., and Mih, W. C., "A Simpler Model for Concentrated Vortices," Experiment in Fluids, Vol. 11,No. 1, 1991, pp. 73–76.

25. Leishman, J. G., Principles of Helicopter Aerodynamics, Cambridge University press, 2006.